MODELING AND ENERGY MANAGEMENT OF HYBRID ELECTRIC VEHICLES

A Thesis

Submitted to the Faculty

of

Purdue University

by

Rishikesh Mahesh Bagwe

In Partial Fulfillment of the

Requirements for the Degree

of

Master of Science in Electrical and Computer Engineering

December 2019

Purdue University

Indianapolis, Indiana

THE PURDUE UNIVERSITY GRADUATE SCHOOL
STATEMENT OF THESIS APPROVAL

Dr. Euzeli Dos Santos Jr, Chair

Department of Electrical and Computer Engineering

Dr. Zina Ben Miled

Department of Electrical and Computer Engineering

Dr. Brian King

Department of Electrical and Computer Engineering

Approved by:

Dr. Brian King

Head of School Graduate Program

This work is dedicated to my parents and my family.

ACKNOWLEDGMENTS

I would like to thank my advisors Dr. Euzeli Dos Santos and Dr. Zina Ben Miled for their guidance and advice. I would also like to thank Dr. Brian King for serving on my committee and for his continuous support during my master degree. The help of Mrs. Sherrie Tucker was invaluable in facilitating the administrative processes related to my academic program.

This project would not have been possible without the support of Allison Transmission Company. I am grateful for the opportunity to work on a real life problem with a practical application. I would like to express my sincere gratitude to Mr. Andy Byerly for his time, mentorship, guidance and knowledge sharing throughout the project. The feedback that I received from Dr. Andrej Ivanco and Mr. Brent Hendrix helped me develop the necessary insight into the application requirements.

The collaborative nature of this project gave me a better appreciation of my teammates Alexander Schoen and John Foust. I am thankful to my officemates Omar Nezamuddin and Maryam Alibeik, for making the office environment friendly and enjoyable.

TABLE OF CONTENTS

Page

LIST OF TABLES

LIST OF FIGURES

SYMBOLS

$\hat{O}_i$	target output
$\tilde{O}_i$	model output
$\hat{O}_{max}$	maximum target output
$\hat{O}_{min}$	minimum target output
S	number of samples
F_{aero}	aerodynamic drag force
A_D	aerodynamic drag coefficient
A	frontal area
v	vehicle speed
ρ	air density
F_{rr}	rolling resistance force
N	normal component of the weight
f_r	coefficient of rolling resistance
C_{sr}	static coefficient of rolling resistance
C_{dr}	dynamic coefficient of rolling resistance
F_{grad}	gravitation force
M_v	Vehicle Mass
g	gravitational acceleration
α	road grade
R_l	road load force
I_{Batt}	battery current
P_{Batt}	battery output power
P_{regen}	regenerative braking power
V_{Int}	battery internal voltage

R_{Int}	battery resistance
Q_{Batt}	total capacity of the battery
T_{batt}	battery temperature
T_{amb}	battery ambient temperature
P_{heat}	battery power lost in heat
C_{cell}	heat capacity of the battery cell
R_{cell}	heat exchange coefficient of the battery cell
$P_{Batt,Req}$	battery power requested
$P_{Eng,Req}$	engine power requested
v_{target}	target vehicle speed
P_{veh}	vehicle power request
P_{Eng}	engine power request
e_{sp}	engine speed
e_{tr}	engine torque
P_{chg}	charging power
K_p	proportional controller gain
SOC_{ref}	reference SOC
D_m	number of miles
T_E	total net energy
F_C	actual fuel consumed
U_f	energy content of one gallon of diesel fuel
Imp	Improvement

ABBREVIATIONS

HEV	Hybrid Electric Vehicle
FCHV	Fuel Cell Hybrid Vehicle
ICE	Internal Combustion Engine
S-HEV	Series Hybrid Electric Vehicle
P-HEV	Parallel Hybrid Electric Vehicle
S/P-HEV	Series/Parallel Hybrid Electric Vehicle
MHEV	Mild Hybrid Electric Vehicle
EMS	Energy Management Strategy
ADAS	Advance Driver Assistant System
V2V	Vehicle to Vehicle
OBS	Optimization-Based Strategy
RBS	Rule-Based Strategy
DP	Dynamic Programming
PSO	Particle Swarm Optimization
ECMS	Equivalent Consumption Minimization Strategy
PRBS	Preliminary Rule-Based Strategy
FRBS	Fuzzy Rule-Based Strategy
CFD	Computational Fluid Dynamics
MVEM	Mean Value Engine Modeling
TCC	Torque Converter Clutch
APP	Accelerator Pedal Position
AD	Aerodynamic Drag
RR	Rolling Resistance
DPL	Discharging Power Limit

CPL	Charging Power Limit
BPP	Brake Pedal Position
SOC	State of Charge
PID	Proportional Integral Derivative
FF	Feed-forward
FB	Feedback
ARBS	Adaptive Rule-Based Strategy
MPGe	Miles per Gallon Equivalent

ABSTRACT

Bagwe, Rishikesh Mahesh. M.S.E.C.E., Purdue University, December 2019. Modeling and Energy Management of Hybrid Electric Vehicles. Major Professor: Dr. Euzeli Dos Santos Jr.

This thesis proposes an Adaptive Rule-Based Energy Management Strategy (ARBS EMS) for a parallel hybrid electric vehicle (P-HEV). The strategy can efficiently be deployed online without the need for complete knowledge of the entire duty cycle in order to optimize fuel consumption. ARBS improves upon the established Preliminary Rule-Based Strategy (PRBS) which has been adopted in commercial vehicles. When compared to PRBS, the aim of ARBS is to maintain the battery State of Charge (SOC) which ensures the availability of the battery over extended distances. The proposed strategy prevents the engine from operating in highly inefficient regions and reduces the total equivalent fuel consumption of the vehicle. Using an HEV model developed in Simulink®, both the proposed ARBS and the established PRBS strategies are compared across eight short duty cycles and one long duty cycle with urban and highway characteristics. Compared to PRBS, the results show that, on average, a 1.19% improvement in the miles per gallon equivalent (MPGe) is obtained with ARBS when the battery initial SOC is 63% for short duty cycles. However, as opposed to PRBS, ARBS has the advantage of not requiring any prior knowledge of the engine efficiency maps in order to achieve optimal performance. This characteristics can help in the systematic aftermarket hybridization of heavy duty vehicles.

1. INTRODUCTION

A vehicle that uses more than one source for propulsion is termed as a hybrid vehicle. Lately, the hybrid electric vehicle (HEV) and the fuel cell hybrid vehicle (FCHV) are becoming popular in the automotive industry. The HEV combines the conventional internal combustion engine (ICE) with an electric motor and a battery storage system. Many companies have been manufacturing and selling HEVs for two decades but the first hybrid car was built in 1898 [1]. The HEV technology is paving the way from gasoline vehicles to pure electric vehicles. A FCHV has a battery power source assisted by compressed hydrogen. The compressed hydrogen energy storage is a cleaner approach compared to gasoline energy storage in hybrid vehicles [2]. In contrast to the high production number of HEVs, fewer FCHV cars are built to date. The rise of electric vehicles, the lack of fueling infrastructure and high hydrogen fuel cost [3] are among the reasons for the low FCHV production.

The two power sources in a hybrid vehicle have their own benefits and drawbacks. A hybrid technology tries to compensate for the drawbacks of one source by using the benefits of the other. For example, in HEVs, the engine does not perform well on duty cycles with high number of stops whereas a battery and an electric motor can propel the vehicle efficiently in such situations [4]. The use of battery power also helps in reducing the emissions. On the other hand, batteries have lower energy density [5] which may limit the range of the vehicle. Although petroleum fuel is the leading cause of greenhouse gases, it has a high energy density and the refueling time is shorter compared to the time needed to charge a battery.

1.1 Classification of HEVs

The engine and the electric motor in a HEV can be connected using different configurations. As a results, the HEVs are classified into three main classes: Series (S-HEV), Parallel (P-HEV) and Series/Parallel (S/P-HEV) [6].

1.1.1 Series HEV

In S-HEV drivetrain, one or multiple motors are coupled to the wheel shaft of the vehicle. The ICE is attached to a generator. The generator is coupled with the battery and the motor. So the ICE assists in either charging the battery or directly propelling the vehicle through the generator and the motor. The advantage of the series configuration is that it can be differential free. That is two motors can be used, one for the right and one for the left side wheels. The engine, motor and generator have to be sized adequately in order to fulfill high power requests by the vehicle. Fig. 1.1 shows the configuration diagram for S-HEV vehicle.

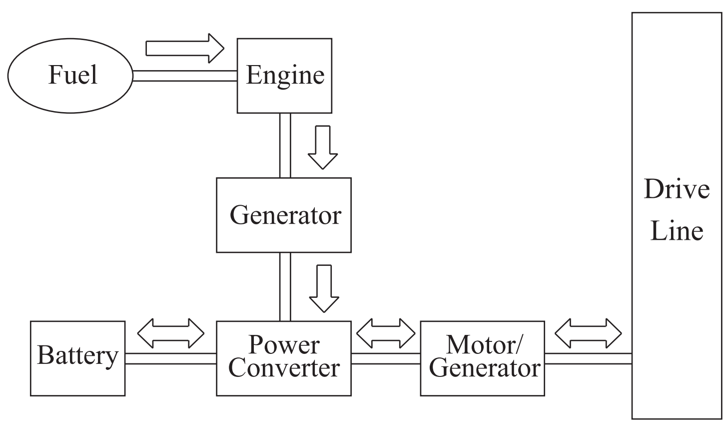

Fig. 1.1. Block diagram of a S-HEV.

1.1.2 Parallel HEV

A P-HEV consists of an ICE and an electric motor coupled to the drive shaft separately. This configuration allows both components to deliver torque to the wheels simultaneously. Unlike S-HEV, a separate generator is not present in a P-HEV. The power requested by the vehicle can be split into engine power request and battery power request. As a result, a downsized engine which is complemented by motor can be used to satisfy vehicle peak power. The power splitting proportion between the components can be optimized for fuel economy. Since the engine is coupled to the drive shaft in a P-HEV, engine speed is determined by the vehicle speed. Whereas for a S-HEV, the engine speed can be adjusted to attain high efficiency for a given torque request. Fig. 1.2 shows the P-HEV configuration and the power flow through the vehicle.

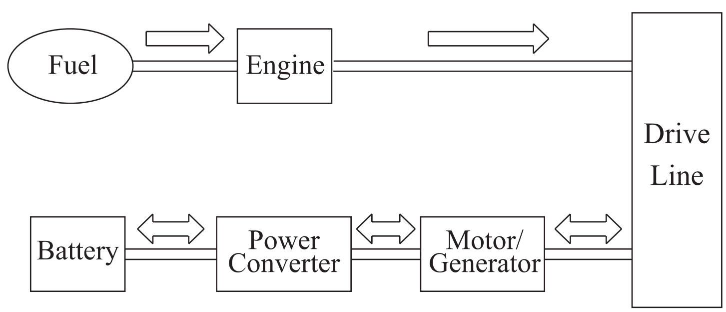

Fig. 1.2. Block diagram of a P-HEV.

1.1.3 Series/Parallel HEV

A S/P-HEV combines the benefits of both the series and parallel configurations. It consists of a generator that connects the ICE to the electric motor and the ICE is also directly connected to the drive shaft. The use of all these components adds complexity and cost to the vehicle.

However, an intelligent power split strategy can help offset the added cost. Commercial vehicles like Toyota Prius and Ford Escape Hybrid use this configuration. Fig. 1.3 shows the S/P-HEV components and their connection.

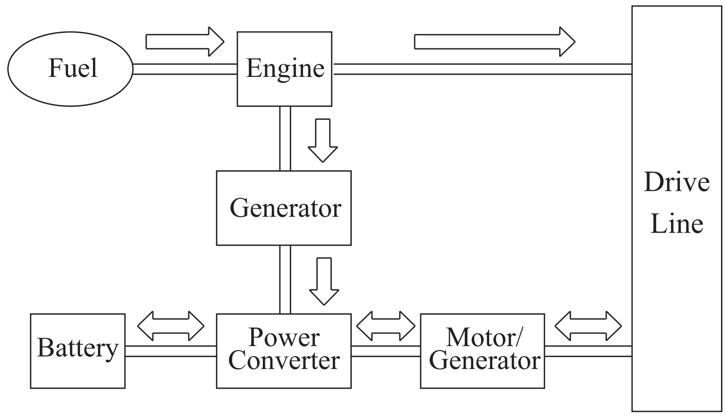

Fig. 1.3. Block diagram of a S/P-HEV.

1.2 P-HEV classification

The P-HEV vehicle can be further classified into four categories based on the relative size of the electric motor with respect to the ICE and battery voltage. They are micro, mild, full and plug-in hybrids [7]. The HEVs with voltage net of 12 V are classified under micro HEVs. The electric motor of micro HEVs has a peak power of 5 kW. It is used to run the engine starter motor and some accessory electrical systems.

The mild HEVs (MHEV) is a category that has become popular due the growing power demand by the vehicle peripheral systems. The development of technologies such ADAS [8], V2V [9] has led to the use of 48 V batteries with electric motors ranging from 5 to 30 kW to supply the sensors, processor cooling systems and some of the high power accessory load like air compressor pumps. Commercial vehicles like Audi A8 have adopted the MHEV technology.

The full P-HEVs have comparable electric motor and ICE sizes. For an ICE of 75 kW, the electric motor can range from 25 to 75 kW in peak power. Unlike the micoror mild- HEVs, the full hybrid system have a pure electric mode where the electric motor can individually propel the vehicle. Toyota Prius vehicles is an example of the full hybrid category.

In Plug-in P-HEVs, the electric motor is larger in size than the ICE. The electric motor is the primary propulsion machine while the ICE assists the electric motor. The main difference between the plug-in hybrids and the full hybrids is the external battery charging capability present in the plug-in hybrids. Chevy Volt is one of the popular plug-in hybrid vehicles.

1.3 Energy Management Systems

In order to achieve high energy efficiency, it is important for a hybrid vehicle to use its power sources optimally. An Energy Management (EM) System controls the power delivered by each of the sources available on-board. Different EM systems are available for HEVs and multiple systems can be implemented on a vehicle depending on its type, class and size. Some of the EM systems are mentioned below:

1.3.1 Regenerative Braking

In conventional ICE vehicles, the car uses friction brakes to decelerate the vehicle. The braking action converts the kinetic energy of the vehicle into heat energy which is wasted. Hybrid vehicles use regenerative braking along with friction brakes to reduce the vehicle speed. The regenerative braking technique converts the kinetic energy of the vehicle in to electric energy which gets stored in the battery and can be reused to propel the vehicle. During regenerative braking, the electric motor of the hybrid vehicle operates as a generator which converts the mechanical energy of the wheels to electric energy. This EM system significantly increases the fuel economy of the HEV over conventional ICE vehicles. HEVs can absorb up to a certain amount of kinetic energy from the vehicle depending on the size of the electric motor and the Amp-hr/hr limit of the battery.

1.3.2 Load scheduling

Different systems may be demanding power simultaneously during the vehicle operation. Some of these systems are time critical where the lack of power can cause noticeable changes in the drivability of the vehicle. For example, ADAS need power to keep operating its sensors like lidar, cameras along with the cooling system that maintains the temperature of the system's microprocessor. Any drop in the power delivered to this system can cause malfunction and endanger the driver's safety. On the other hand, some systems in the vehicle are not critical. An example of such system is the vehicle's air conditioning system. A load scheduling EM systems only operates the non-critical systems if delivering power to these systems allows the ICE and the motor to still operate in their efficient regions.

1.3.3 Engine Start/Stop

With the growing number of cars on road, vehicles spend an increasing amount of time idling in the city traffic. The ICE consumes some fuel to keep the engine idling in such situations. Completely turning off the engine at a stop in a conventional ICE vehicles leads to uncomfortable starts and lagging responses from the vehicle. The starter motors in the conventional ICE are not big enough to enable a smooth start of the engine. The HEV have more powerful motors that can crank the engine faster. Therefore this EM system can help cut down the fuel that is wasted by stopping the engine when the vehicle is at a stop.

1.3.4 Power split

The major advantage of a P-HEV or S/P-HEV is that the total power requested by the vehicle can be split between the ICE and the electric motor. The ICE fuel map has inefficient regions, so delivering certain power request from the ICE is non-economical. Using the electric motor to supply some of the power in these cases is beneficial and may yield higher fuel economy. If power demand is low, ICE can produce more power thus moving to an efficient operating region and use the excess power produced to charge the battery.

The power split opportunity in P-HEV allows it operate in five modes, they are, a) Motor only propulsion, b) Engine only propulsion, c) Motor Assist, d) Engine charging the battery, and e) Regenerative braking. A strategy that can optimize the power split between the sources of power in an P-HEV is needed. Several strategies have been previously proposed. This thesis describes an online optimization strategy for P-HEVs. The proposed approach is easier to implement and achieves better fuel economy without the knowledge of the engine maps.

1.4 Energy Management Strategy

An Energy Management Strategy (EMS) is an algorithm that decides the amount of power delivered by each of the source. It is an important aspect of fuel economy and emission control in HEVs. The objective of the EMS is to efficiently use the two sources of energy available in the HEV. The EMS strategies broadly fall under two categories: optimization-based (OBS) and rule-based (RBS) strategies [10].

The OBS category relies on several optimization techniques including dynamic programming (DP) [11], particle swarm optimization (PSO) [12] and equivalent consumption minimization strategy (ECMS) [13]. When the DP technique is used, the problem is discretized over time into a sequence of optimization sub-problems. To obtain a global optimum, these sub-problems are then solved by using backward induction. Because it uses backward induction, this technique requires a priori knowledge of the entire duty cycle in order to optimize fuel economy in HEVs. PSO also needs full a priori knowledge of the entire duty cycle. When PSO is used as the optimization technique, the objective function is fuel consumption. Particles represent potential solutions that minimize the objective function and these solutions are updated at each iteration of PSO according to the current lowest fuel consumption solution for each particle as well as the current lowest fuel consumption solution across all particles.

The third OBS technique, ECMS, tries to overcome the limitation of the a priori knowledge of the entire duty cycle underlying the DP and PSO techniques by converting the global optimization problem into a local problem. The global objective function is transformed into a local optimization problem by including a fuel equivalent cost for use of the battery. ECMS can be implemented online. However, establishing the fuel equivalent cost factor for the conversion of the battery usage into equivalent fuel cost requires substantial calibration in order for this approach to generate optimal solutions. Moreover, the resulting solutions are often duty cycle-specific [14].

The second category of EMS strategies is the RBS category. The RBS strategies are computationally more efficient than the OBS strategies and therefore can be easily implemented online. One of the most widely adopted rule-based EMS is the preliminary rule-based strategy (PRBS) which was introduced in [15] and [16]. PRBS is based on the engine efficiency map of the vehicle and is powertrain-specific. The fuzzy rule-based strategy (FRBS) [17] is another RBS technique that is not specific to a given powertrain. However, while still practical for online deployment, it is computationally more complex than PRBS.

In general, RBS is the EMS strategy of choice for commercial and practical applications. The OBS strategies are typically used to gain insight into the behavior of the vehicle powertrain. The design rules derived from the observations of this behavior are then incorporated into a RBS strategy. For example, DP, support vector machines and neural networks have been adapted to a rule-based online implementation in [11], [18] and [19], respectively. The RBS energy management strategy has been successfully implemented in various commercial vehicles such as the Toyota Prius [20]. RBS is computationally efficient and does not rely on the knowledge of the entire duty cycle. However, it still may require extensive tuning by experts based on engine efficiency maps and its optimality may not be guaranteed.

This thesis presents an online RBS energy management strategy for HEVs which can be tuned without the knowledge of the engine efficiency map. It can prove to be effective in aftermarket hybridization process where typically the engine maps of the conventional vehicles are not readily available. The proposed strategy is suitable for a parallel HEV and can achieve higher fuel economy than PRBS strategy. Moreover the proposed strategy is computationally efficient.

2. MODELING

Modeling physical systems by using a computational framework is a widely used technique. It facilitates the analysis of the physical systems during the various phases of the systems′ life cycles. Because of their underlying complexity, models are usually developed for a specific need and each model has advantages and limitations. Indeed, as reported in [21], "All models are wrong, some are useful". Therefore, the models of physical systems are evaluated based on their accuracy in faithfully reproducing the physical system′s behaviors, their generalizability to a family of physical systems, and their complexity.

Current modeling techniques range from first principle modeling (e.g., CFD [22], Block Diagram [23]) to data-driven modeling (e.g., Neural Networks [24], System Identification [25]). In the automotive industry, conducting tests on physical prototypes during the design or adaptation phases of the product may neither be practical nor cost effective. For instance, in order to incorporate a new control strategy, a digital vehicle model, instead of the physical prototype, may be used to assess the impact of the new strategy on the entire vehicle. This process is commonly followed in the automotive industry [26], [27], [28], [29], [30]. The flexibility afforded by the digital model can result in significant time and cost saving. Moreover, with the emergence of connected vehicles, one can anticipate that digital models will be used to enhance the performance of individual vehicles or a fleet of vehicles while in use. For instance, a new configuration for a fleet of vehicles can be tested on the digital model for improved fuel economy on a specific route and then applied to the actual vehicles. Researchers have been harvesting data from the vehicles on road ([31], [32]) which would then facilitate the development of a vehicle digital clone [33].

Developing an accurate digital model for a vehicle requires the integration of the models for the underlying components of the vehicle. The vehicle model developed in this study consists of the combination of models for a) the engine, b) the transmission, the torque converter clutch and c) the vehicles interaction with the road. Models for the aforementioned components may be heterogeneous where each model is based on a different computational technique. Additionally, a driver model is also developed. It consists of a controller that allows the vehicle plant model to follow a reference duty cycle.

2.1 Engine

The Engine modeled in this research is a diesel fueled V6 type engine with a maximum torque of 2100 $N.m$ at 1200 rpm and a maximum rated power of 321.44 kW. Traditionally, the engine component of the vehicle is modeled using 1-dimensional computational fluid dynamics (CFD). This technique is used in commercial software such as GT-Power [34]. It treats the engine as a piping system and the associated model focuses on the fluid dynamics in the engine manifolds, valves and the cylinder body [35]. The goal of CFD is to capture the variances in the parameters within an engine cycle. Another widely used engine modeling technique is the Mean Value Engine Modeling (MVEM). This technique describes the average engine behavior over several engine cycles [36]. Compared to CFD, MVEM is less accurate but computationally more efficient. There are several techniques to build a MVEM model like lookup tables [37] and Neural Networks [38].

In this thesis, the Engine (Fig. 2.1) is modeled as a combination of two engine maps, EM1, and EM2 following the approach described in [39] and [40]. The input of the model consist of the engine power request (P_{eng}) and the transmission input speed. The output are the engine torque and the engine fuel rate.

EM1 defines the maximum engine torque curve. It is used to limit the engine torque request derived from the engine speed and the engine power request. EM2 defines the engine fuel rate as a function of the engine speed and the engine torque. These engine maps represent the operational specifications of the engine and are

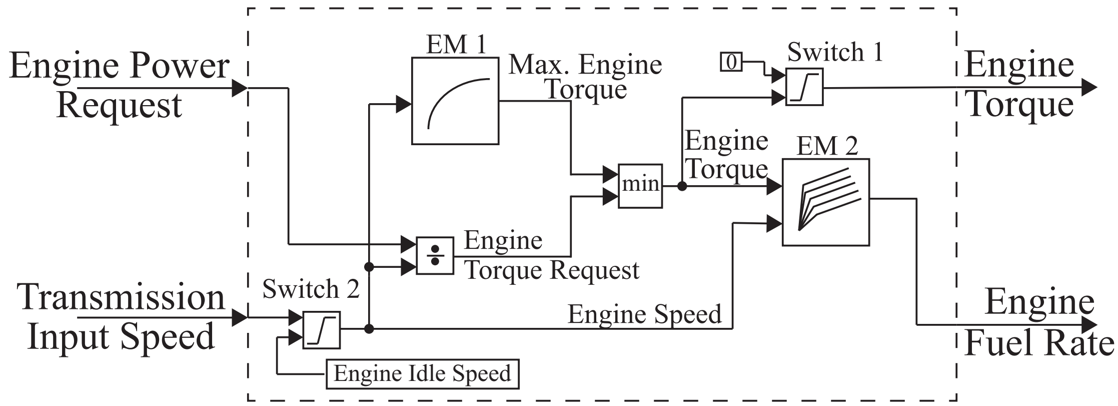

Fig. 2.1. Engine model.

measured during performance testing of the engine. In addition to the above two engine maps, the engine model also emulates the behavior of the torque converter clutch (TCC) by using two switches (Fig. 2.1). Switch 1 forces the engine propulsion torque to zero and switch 2 holds the engine speed constant when the engine is in the idle state. The transmission input speed has a range from 0 to 2200 rpm. The output engine torque and engine fuel rate have a range from -250 to 2100 $N.m$ and 0 to 125 Lph, respectively. The engine maps and the logic for the TCC replicate the expected operational behavior of the engine.

2.2 Transmission

The transmission helps the engine operate in an efficient engine speed range. An automatic transmission system is a discrete system. That is, there is no linear transition between the states of the transmission. In the proposed vehicle model, the Simulink® Stateflow® toolbox was used to simulate the finite state machine governing the transmission gear box. Each state in the transmission model represents a particular gear ratio.

The transmission being modeled in this study is a 6-speed automatic transmission. The transition between the states is guided by the transmission shift-schedules. These schedules are different for up-shifting and down-shifting which creates a hysteresis phenomenon that avoids rapid back and forth switching between two adjacent gear states [41]. The shift schedules depend on the vehicle speed and the APP. In order to create the shift-schedule maps from the real data, the vehicle speed and the accelerator pedal position (APP) are plotted for different gear states as shown in Fig. 2.2. The boundaries of these gear state regions form the transmission shift-schedule maps. The data used to build the shift schedule maps was collected from a vehicle that has the same transmission as the target HEV vehicle. Fig. 2.2 shows the derived downshift and upshift schedule maps for the vehicle under consideration.

The complete diagram of the transmission model is shown in Fig. 2.3. The input of the transmission model includes the vehicle speed and the APP. The output is the *gear ratio*. A function block, implemented in MATLAB®, is used to generate the upshift and downshift schedules. Depending on the value of APP, this function

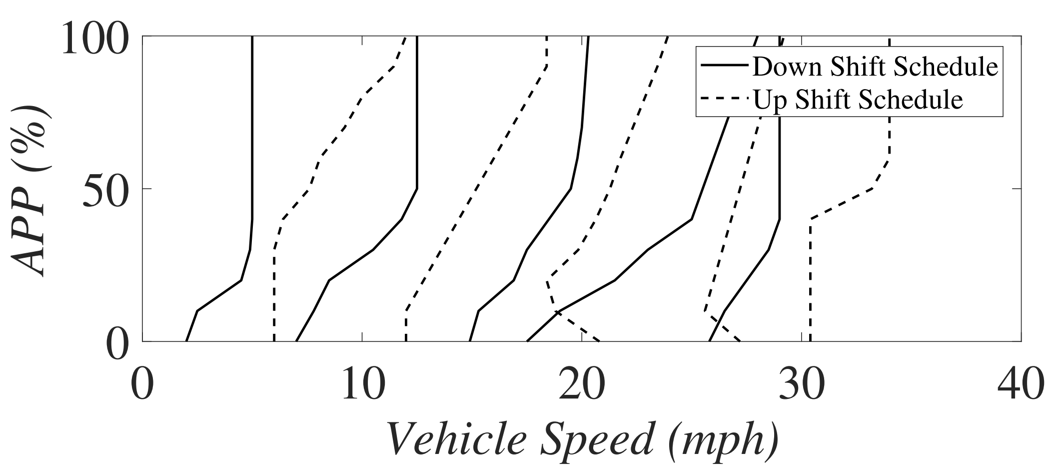

Fig. 2.2. Transmission shift schedule maps.

block communicates two sets of 5 vehicle speeds each to the state flow block shown in Fig. 2.3. These sets represent the transition speeds for the current APP. The State flow block then determines the appropriate gear by comparing the current vehicle speed with the transition speeds. The gear ratio associated with each gear was also determined from the dataset. It is calculated by dividing the transmission output speed by the turbine speed. The transmission torque converter clutch is not modeled as part of the transmission model. However, it is included in the integrated vehicle model as discussed in Section 2.5.

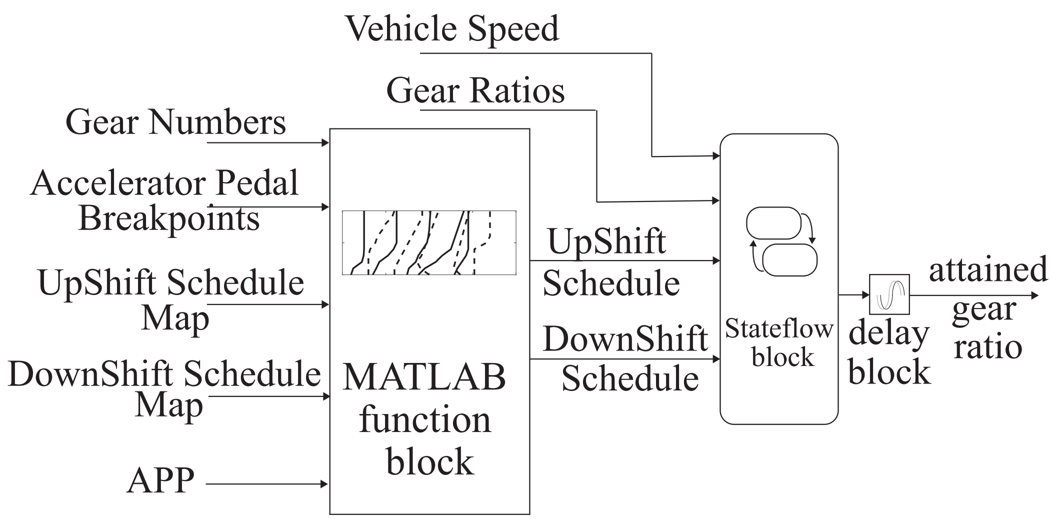

Fig. 2.3. Transmission Model.

The transport delay block in Fig. 2.3 emulates the time taken by the transmission to engage and disengage the clutch plates while changing gears. During testing, the transmission model is initialized with the shift-schedules maps and this delay is set to 1sec.

The transmission model was validated using eight duty cycles. The vehicle speed and APP are extracted from the dataset and used as input to the transmission model. The $transmission\, gear$ predicted by the model is then compared to the actual gear value recorded in the dataset using the following equation:

$$\%\, error = \frac{1}{S} \cdot \frac{\sum_i \mid \hat{O}_i - \tilde{O}_i \mid}{\hat{O}_{max} - \hat{O}_{min}} \times 100 \tag{2.1}$$

where $\hat{O}_i$ is the target output, $\tilde{O}_i$ is the corresponding model output and S is the number of samples. The error (2.1) between the predicted gear and the actual gear across the eight duty cycles is 5.7%. A sample of both simulated and actual gears for a period of 500 sec. is shown in Fig. 2.4. The neutral gear state is not shown in Fig. 2.4 because, the vehicle does not come to an engine-off stop during the trips.

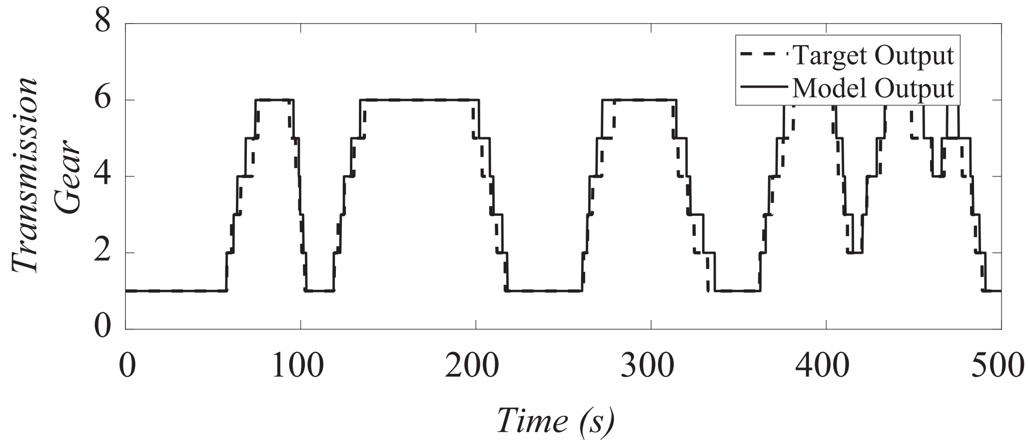

Fig. 2.4. Predicted versus actual transmission gear.

2.3 Vehicle Road Load Model

The power generated in the engine and the battery is delivered to the tires of the vehicle through the powertrain. The vehicle road load model emulates the interaction between the vehicle and the road. While the two power sources are propelling the vehicle in the forward direction, there are opposing forces acting on the vehicle, namely, the aerodynamic drag and the rolling resistance. The vehicle has to overcome these forces in order to move forward. The free body diagram of the forces acting on the vehicle is shown in Fig. 2.5.

The aerodynamic drag force (F_{aero}) is produced when the vehicle is trying to cut through a volume of air. This force has a major impact on vehicles especially, as in the case of this study, for heavy-duty trucks and buses because of their large fontal areas. In general, it is difficult to accurately express F_{aero} because of the complex interaction between the air flow and the body of the vehicle [42]. Instead, a semi-empirical equation for the aerodynamic drag (F_{aero}) is used as shown in (2.2).

$$F_{aero} \approx \frac{1}{2} \cdot A_D \cdot \rho \cdot A \cdot v^2 \tag{2.2}$$

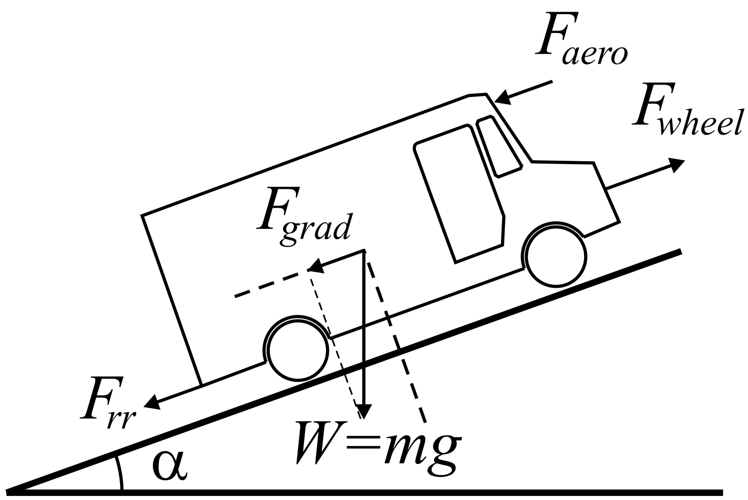

Fig. 2.5. Vehicle Free Body diagram.

where A_D is the aerodynamic drag coefficient which is determined empirically for each vehicle [43], ρ corresponds to the air density, v is the velocity of the vehicle and A is the frontal area of the vehicle.

Unlike the aerodynamic force whose effects are considerable at higher vehicle speeds, the rolling resistance force (F_{rr}) is consistently significant throughout the operation of the wheels. It is affected by the road material and the weight of the vehicle on the wheels. It is also affected by the composition of the rubber material of the tires as well as their design, temperature, and inflation pressure. Using the above parameters, the rolling resistance (F_{rr}) can be as expressed as follows [42]:

$$F_{rr} \approx f_r \cdot N \tag{2.3}$$

where N is the normal component (i.e., with respect to the ground) of the weight force on the wheels and f_r is the coefficient of rolling resistance. The parameter f_r is dimensionless and reflects the physical properties of the tire and the ground. An expression for f_r is provided in [44] and repeated here in (2.4) for convenience.

$$f_r \approx C_{sr} + (3.24) \cdot C_{dr} \cdot (\frac{v}{100})^2 \tag{2.4}$$

where C_{sr} and C_{dr} represent the static and dynamic coefficients of the rolling resistance, respectively. These coefficients vary with the inflation pressure in the tires.

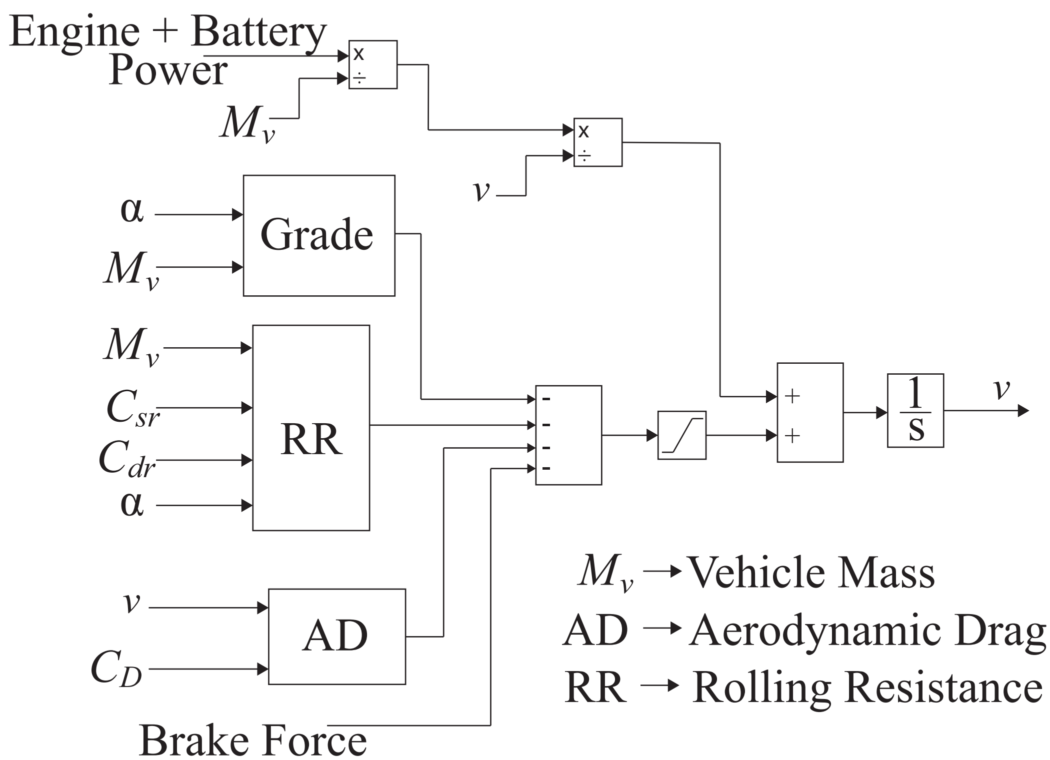

Fig. 2.6. Vehicle Road Load Model.

When a vehicle is on a road with a non-zero grade, a portion of the gravitational force either opposes the vehicle motion or helps it. According to [42], the gravitation force (F_{grad}) can be expressed as follows:

$$F_{grad} = M_v \cdot g \cdot sin(\alpha) \tag{2.5}$$

where, α is the grade of the road and $M_v \cdot g$ is the total weight of the vehicle.

By taking into account all of the above forces, the total road load force (R_l) on the vehicle can be expressed by:

$$R_l \approx \frac{1}{2} \cdot A_D \cdot \rho \cdot A \cdot v^2 + f_r \cdot N + M_v \cdot g \cdot sin(\alpha) \tag{2.6}$$

Equation (2.6) is the basis of the Simulink® road load model implementation in this research. This model is shown in Fig. 2.6. The maximum brake force is the service brake force applied to the vehicle when the brake pedal is pressed at a 100%. Unfortunately, the dataset used in this study did not record a continuous brake pedal position (BPP). Instead, the BPP was recorded as a binary value corresponding to on/off. Therefore, the maximum brake force value was assumed to best fit the duty cycle.

The vehicle road load model was also tested using a randomly selected trip from the dataset. The input to the vehicle road load model (i.e. propulsion power, road grade, vehicle mass) were taken from the real data for the purpose of this testing. A sample of the simulation results is shown in Fig. 2.7. The error for the vehicle speed over the 500 sec. testing duration is 3.8%.

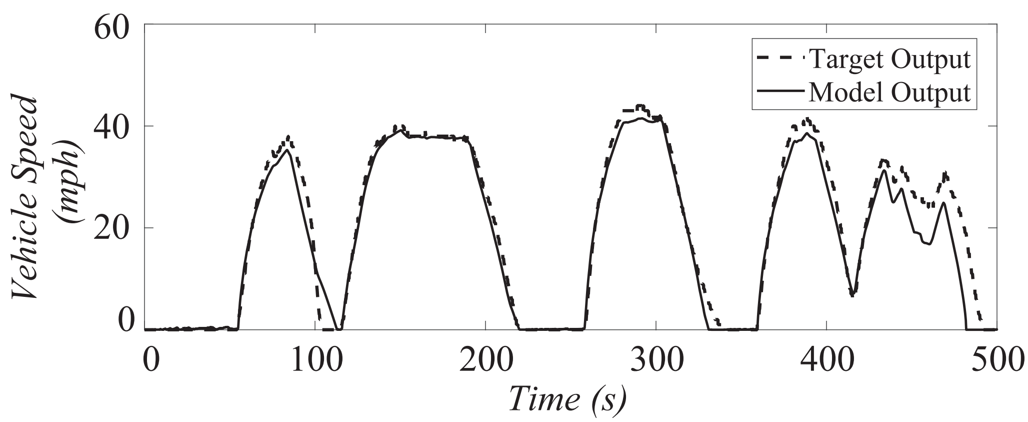

Fig. 2.7. Actual versus predicted vehicle speed.

2.4 Battery Model

The battery pack in the HEV is modeled as a combination of series and parallel cell batteries. The circuit used to model a single cell battery is shown in Fig. 2.8.

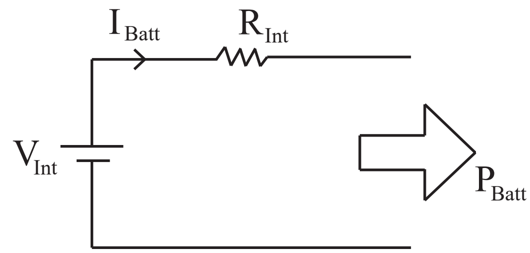

Fig. 2.8. Battery cell model.

The battery discharging current is assumed to be positive in the remainder of the thesis. As a result, the battery discharging power is also assigned a positive battery power value. Therefore, if the battery is discharging, both the battery power (P_{Batt}) and the battery current (I_{Batt}) have positive values. In addition to delivering power to the vehicle, the battery can also absorb power (P_{regen}) from the vehicle during regenerative braking. Since the battery is charging during regenerative braking, the regenerative power (P_{regen}) takes on negative values.

According to [45], the battery current during discharging is given by

$$I_{Batt} = \frac{V_{Int} - \sqrt{V_{Int}^2 - 4R_{Int}P_{Batt}}}{2R_{Int}} \tag{2.7}$$

where, V_{Int} and R_{Int} are the battery internal voltage and resistance, respectively. The battery current during charging is negative and follows the same definition in (2.7) with P_{regen} substituted for P_{Batt}.

The state of charge (SOC) of the battery represents the amount of energy left in the battery. As defined in [45], the relationship between SOC and I_{Batt} is given by the coulomb counting differential equation shown below:

$$\frac{dSOC(t)}{dt} = \frac{I_{Batt}}{Q_{Batt}} \tag{2.8}$$

where, Q_{Batt} is the total capacity of the battery.

The internal parameters, V_{Int} and R_{Int} of the battery vary with changing levels of SOC and battery temperature (T_{batt}). In the battery model (Fig. 2.9), these relationships are represented by using two look-up tables (LT). These look-up tables LT1 and LT2, obtained from [46], define V_{Int} and R_{Int} as a function of SOC and T_{batt}, respectively. The battery ambient temperature (T_{amb}) is kept constant for all the simulations in this study. The battery temperature varies with T_{amb} and the heat generated in the battery. The heat equation (2.9) shows the relationship between the change in battery temperature its heat capacity and heat generated by R_{Int}.

$$C_{cell} \cdot \frac{dT_{batt}}{dt} = -\frac{T_{batt} - T_{amb}}{R_{cell}} + P_{heat} \tag{2.9}$$

where C_{cell} is the heat capacity of the cell and R_{cell} is the heat exchange coefficient of the battery obtained from [46].

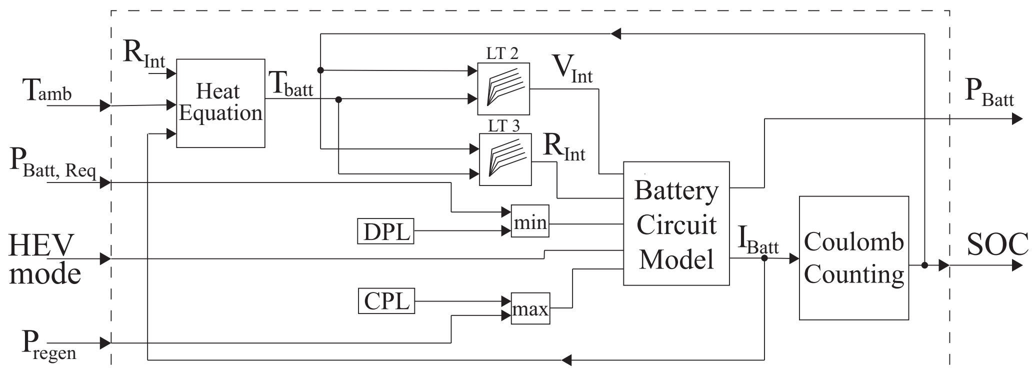

Fig. 2.9. Battery model. The $HEVmode$ indicates whether the battery is charging or discharging.

2.5 Integrated Vehicle Model

The engine, transmission, road load and battery models introduced in the previous sections were combined in the integrated vehicle model shown in Fig. 2.10.

The power generated by the engine and battery model is fed to the road load model which, in turn, defines the speed of the vehicle. The vehicle speed is then converted to the transmission output speed. The transmission model calculates the gear ratio which, when multiplied by the transmission output speed, provides the transmission

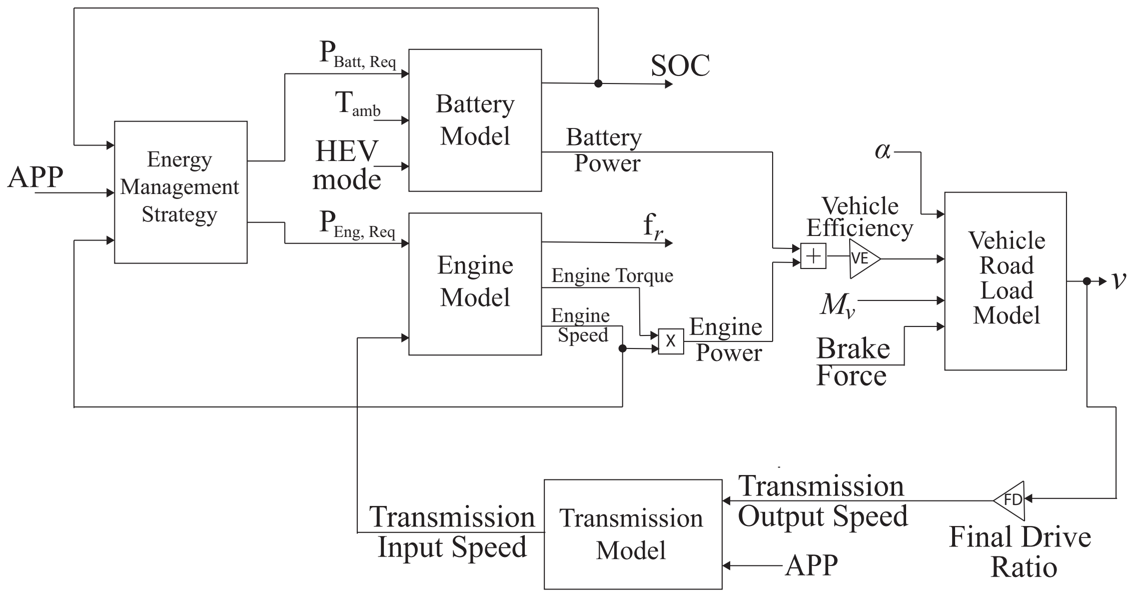

Fig. 2.10. Integrated Vehicle Model.

input speed. In the integrated vehicle model, the torque or the power information propagates from the engine to the vehicle road load model while the speed propagates in the reverse direction.

The transmission input speed is related to the engine speed through the torque converter clutch (TCC). The TCC divides the vehicle model into two states. The vehicle model is in the idling state when the TCC is disengaged and it is in the active state when the TCC is engaged. The engine speed is equal to the Transmission Input Speed during the active state, whereas it is equal to a predefined engine speed during the idling state. In the vehicle model, the TCC is emulated using two switches: the first switch is on the torque/power path (Switch 1) and the second switch (Switch 2) is on the speed path as shown in Fig. 2.10. Switch 1 limits the power given to the vehicle road load model when TCC is disengaged and the engine is idling. Switch 2 limits the speed of the engine to an idling speed.

In the real world, the vehicle has internal losses due to the friction present between two moving parts in the drivetrain,

- pumps present in the engine and transmission support systems,
- the accessories connected to the vehicle (e.g., air compressor)

These losses have to be accounted for in the sub-models described in the previous sections. As stated in [47], the drivetrain losses are generally in the range of 8% to 12%. The accessory losses are assumed to be around 3%. Therefore, the total losses are approximated at 15% in this study. This vehicle efficiency (i.e. 85%) is shown in Fig. 2.10 on the power path between the two power sources and the vehicle road load model. The external input of the vehicle model consists of the APP and the $road\,grade$. The overall outputs of the model are the $fuel\,rate$ and SOC.

2.6 Driver Model

The vehicle model needs to be actuated according to a duty cycle which is normally dictated by the driver. For the purpose of this study, a driver model that replicates the actions of a driver was implemented. The driver model controls the integrated vehicle model.

Driver models are constructed for different purposes. As explained in [48], the purpose can be either descriptive or motivational. The latter predicts the behavior of the driver whereas the former describes a given driving activity. An example of a motivational model is presented in [49]. In this study a dataset representing 10 drivers was used to develop a predictive model that can improve the lane departure warning system. The driver model can be developed by using various techniques. For instance, neural networks, fuzzy control and optimal control theory are used in [50], [51] and [38], respectively.

The input of the driver model in this thesis includes the target duty cycle and the corresponding road grade from the real dataset. The model is implemented as a combination of a feedback and a feedforward control (Fig. 2.11). The feedback path has two lead-lag controllers which examine the errors in the vehicle speed and the vehicle acceleration. Since the aim of the proposed model is to estimate average fuel economy, the feedback controller also monitors the error in the distance and proportionally increases the output of the feedback block. The feedforward module performs the inverse calculations of the vehicle model. It calculates the APP needed to achieve the necessary vehicle speed in the immediate future. The output of the driver model consists of the APP and the BPP. These signals are used to drive the integrated vehicle model.

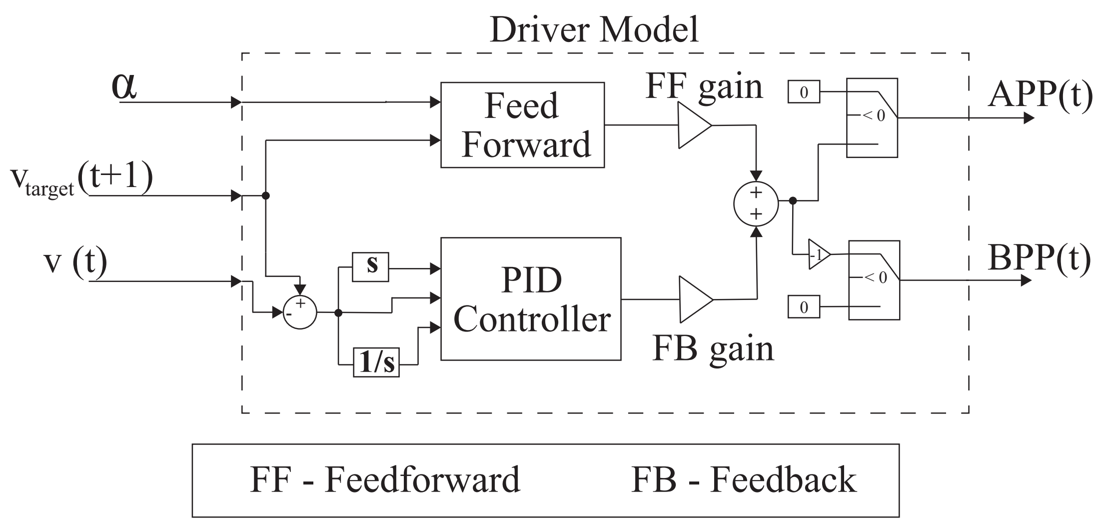

Fig. 2.11. Driver Model block diagram.

3. ENERGY MANAGEMENT STRATEGY

An EMS is necessary in order for an HEV to supply the desired vehicle power, $P_{veh}(t)$, at the wheels. The role of the EMS is to efficiently splits $P_{veh}(t)$ into a request for engine power, $P_{Eng}(t)$ and a request for battery power, $P_{Batt}(t)$. The split always adheres to the following relation:

$$P_{veh,req}(t) = P_{Batt,req}(t) + P_{Eng,req}(t) \tag{3.1}$$

Table 3.1.: Definition of EMS parameters.

Parameters	Definition
$e_{sp}(t)$	Engine speed at time t.
$e_{tr}(t)$	Engine torque at time t.
$P_{veh,req}(t)$	Desired vehicle power at time t.
$P_{Batt,req}(t)$	Requested battery power at time t.
$P_{Eng,req}(t)$	Requested engine power at time t.
P_{12}	Defines the boundary curve between regions 1 (motor) and 2 (engine) in the engine efficiency map. For the PRBS controller, this value is constant (i.e., $P_{12} = 100kW$). For the ARBS controller, $P_{12}(t)$ varies as a function of time.
P_{12}^{+}, P_{12}^{-}	Defines the maximum/minimum power for the boundary between regions 1 (motor) and 2 (engine) for the ARBS controller.
P_{23}	Defines the boundary curve between regions 2 (engine) and 3 (motor+engine) in the engine efficiency map. It is a constant (i.e., $P_{23} = 250kW$) for both the PRBS and ARBS controllers.

continued on next page

Table 3.1.: *continued*

Parameters	Definition
P_m	Constant margin for P_{12} and P_{23} in the PRBS controller.
$SOC(t)$	SOC of the battery at time t.
SOC_{min}, SOC_{max}	Minimum/Maximum allowable SOC for the battery
SOC_m	Constant margin for SOC_{min} and SOC_{max} in the PRBS controller.
SOC_{ref}	Reference value for the SOC that the ARBS strategy tries to maintain.
P_{chg}	Constant predefined amount of power which is supplied by the engine in order to charge the battery.
K_p	Gain of the proportional controller in the ARBS strategy.

In this section, we first review the approach used by the PRBS strategy [15] to split the desired vehicle power into engine power and battery power. This approach is then compared to the split approach of the proposed ARBS. The parameters used to describe both EMS strategies are defined in Table 3.1.

3.1 Preliminary Rule-Based Strategy

The RBS strategy was initially introduced in 1997 [52]. Subsequently, a PRBS strategy for a parallel hybrid heavy-duty truck was proposed in [15]. The PRBS strategy relies on the efficiency map of the target engine which consists of three operating regions as shown in Fig. 3.1. The power values P_{12} and P_{23} define the boundaries between operating regions 1 and 2 and operating regions 2 and 3, respectively. For PRBS, $P_{12} = 100kW$ and $P_{23} = 250kW$. These values are determined experimentally with the purpose of constraining the engine to high efficiency operating levels.

The PRBS strategy is implemented in a controller. At any time during the operation of the vehicle, the desired vehicle power $P_{veh}(t)$ and $SOC(t)$ values are fed to the PRBS controller. The $SOC(t)$ value is generated by the battery model whereas $P_{veh}(t)$ is calculated based on the $APP(t)$ output of the driver model using a vehicle pedal progression map. Based on this information and the value of the current engine speed ($e_{sp}(t)$), the controller first identifies the region of $P_{veh}(t)$ on the engine efficiency map (Fig. 3.1) and then defines the power split (3.1) according to the following rules:

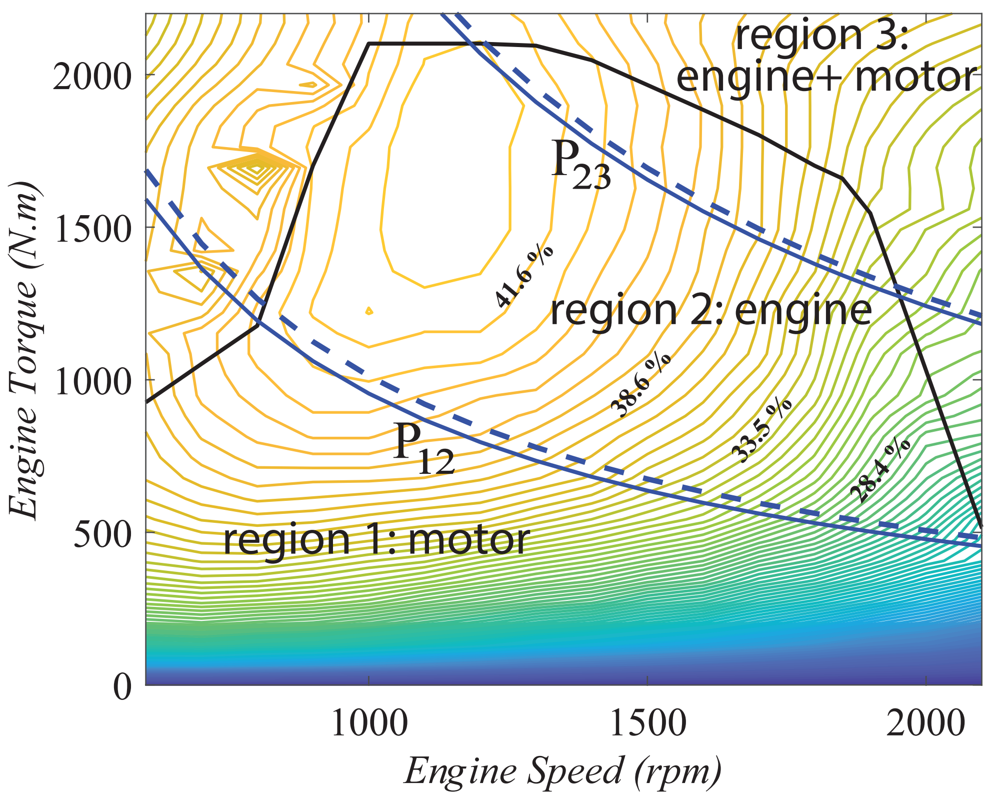

Fig. 3.1. Engine efficiency map with the three operating regions used in the PRBS strategy. The dashed curves represents the margin P_m for P_{12} and P_{23} as the vehicle switches from one region to another. The solid black line is the maximum torque curve of the engine. The percentages represent the efficiencies of the engine.

1. $P_{veh}(t)$ in region 1:

    - If $SOC(t) > SOC_{min}$, then all the requested $P_{veh}(t)$ is provided by the battery. This region is labeled as the motor region.
    - Otherwise, the engine supplies $P_{veh}(t) + P_{chg}$, where $P_{veh}(t)$ is delivered to the driveline and P_{chg} is used to recharge the battery.

2. $P_{veh}(t)$ in region 2: In this case $P_{veh}(t)$ is delivered by the engine irrespective of the value of $SOC(t)$. This region is labeled as the engine region.

3. $P_{veh}(t)$ in region 3:

    - If $SOC(t) < SOC_{min}$, $P_{veh}(t)$ is supplied by the engine.
    - Otherwise, the engine delivers P_{23} and the balance of the requested power (i.e., $P_{veh}(t) - P_{23}$) is provided by the battery.

In addition to the above operating modes, the HEV absorbs power to recharge the battery while it is decelerating. This process is called regenerative braking. When the requested power is negative (i.e., $P_{veh}(t) < 0$), the PRBS controller compares $SOC(t)$ to SOC_{max}:

- If $SOC(t) > SOC_{max}$, then no power is absorbed by the battery and the vehicle has to slow down using the friction brakes.
- Otherwise, the battery is recharged through regenerative braking. That is, the motor in the HEV acts as a generator, absorbs the net vehicle inertia and helps it to stop.

Finally, in order to prevent high frequency switching between operating regions, the power region boundary and the SOC are adjusted by a constant margin. P_{12} and P_{23} are adjusted by the constant margin $P_m = 6kW$. The boundary curves derived from these step changes are shown by dashed lines in Fig. 3.1. The margin SOC_m for SOC_{min} and SOC_{max} is set to 5%. These margins are used in the rules of the PRBS controller when establishing the operating region (i.e., $P_{12} + P_m$ and $P_{23} + P_m$) and when comparing $SOC(t)$ to either SOC_{min} or SOC_{max} (i.e., $SOC_{min} + SOC_m$ and $SOC_{max} + SOC_m$) in order to maintain the current operating region of the vehicle, thereby limiting switching between regions 1 and 2 and between regions 2 and 3. Fig. 3.2 shows the PRBS algorithm.

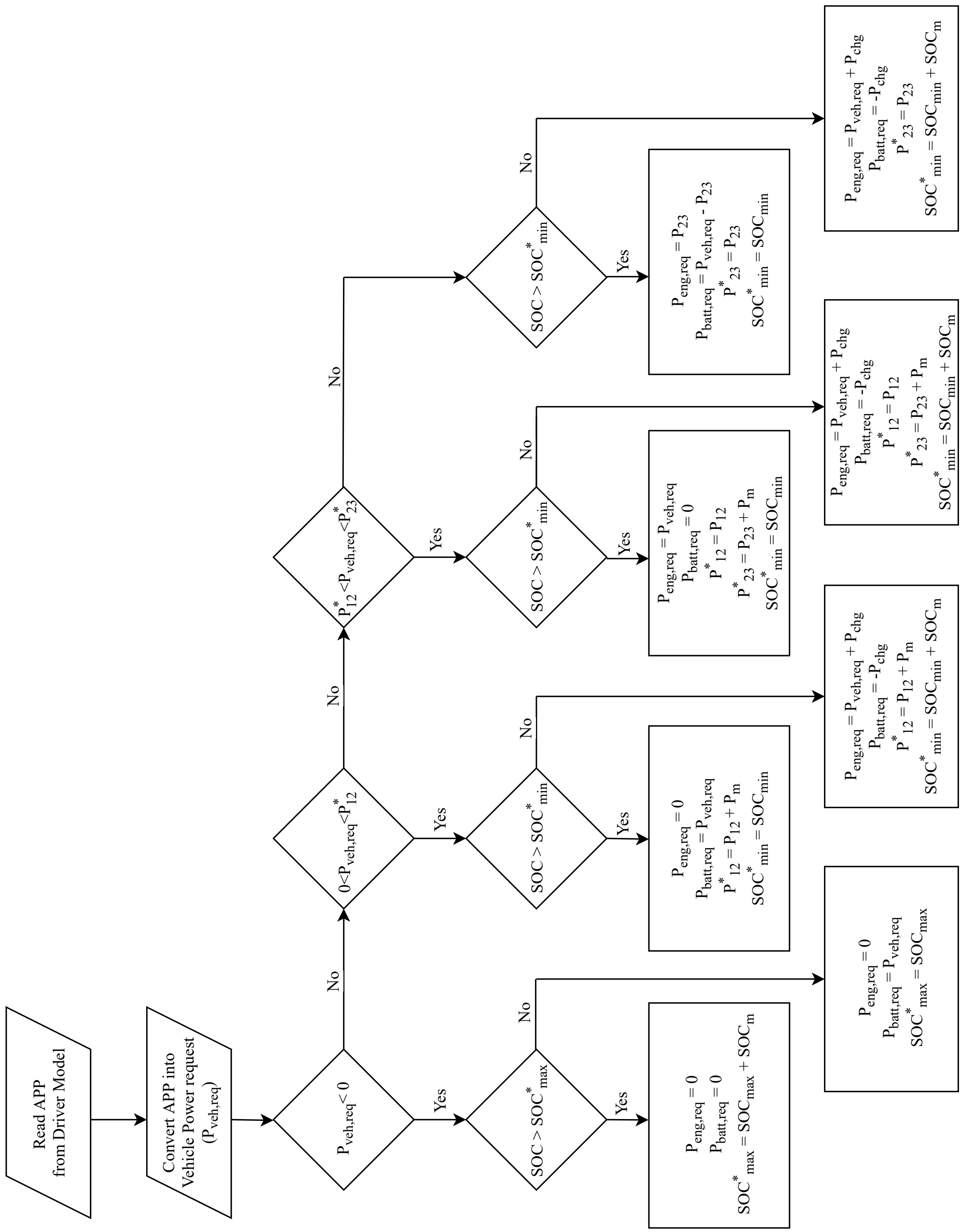

Fig. 3.2. Algorithm for PRBS strategy.

3.2 Adaptive Rule-Based Strategy

The PRBS strategy described above is easy to implement online. However, the strategy suffers from a main limitation. Indeed, the same region boundaries are maintained across all duty cycles. Therefore, if $P_{veh}(t)$ for a given duty cycle mostly falls in region 1, the battery will be used extensively causing its quick depletion. This will force the vehicle to operate in region 2 and rely primarily on the engine even if $P_{veh}(t)$ lies in an inefficient operating region for the engine. This limitation is particularly detrimental over extended travel distances. Moreover, this scenario will occur despite the fact that PRBS allows for a margin P_m on P_{12} and P_{23} and a margin SOC_m on SOC_{min} and SOC_{max}. These PRBS margins are constant, limited in range and intended to reduce the frequency of switching between operating regions.

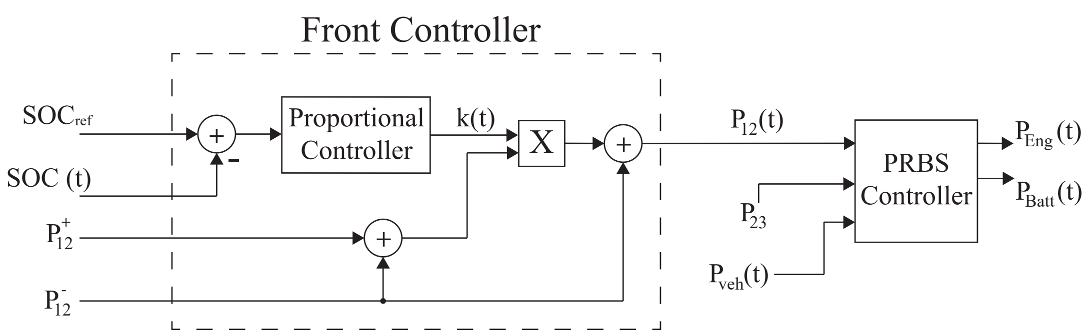

Fig. 3.3. ARBS controller.

The main contribution of the proposed ARBS approach is that it introduces an additional controller in front of the PRBS controller that dynamically adjusts P_{12} at each time step according to the duty cycle. The output of this front controller is fed into the traditional PRBS controller described in the previous subsection as shown in Fig. 3.3.

The time variant $P_{12}(t)$ in ARBS is defined as follows:

$$P_{12}(t) = k(t) \cdot (P_{12}^{+} - P_{12}^{-}) + P_{12}^{-} \tag{3.2}$$

where P_{12}^{-} and P_{12}^{+} are maximum and minimum boundary values for $P_{12}(t)$ (Table 3.1). Their values are set to $100Kw$ and $150Kw$, respectively. These boundary values are determined experimentally based on the engine map. Since region 1, the motor region, represents a low efficiency operating region for the engine and region 2, the engine region represents a high efficiency operating region for the engine, P_{12}^{-} and P_{12}^{+} are selected to clearly delineate these regions.

The ARBS also tries to maintain the battery SOC close to a reference value SOC_{ref} which is set to 50%. The value of SOC_{ref} is determined based on the rated operating range of the battery. It is compared to $SOC(t)$ by using a proportional controller which is embedded within the front controller. The output of the proportional controller, $k(t)$, is used to derive $P_{12}(t)$ in (3.2). $k(t)$ is defined as follows:

$$k(t) = 0.5 - K_p \cdot (SOC(t) - SOC_{ref}) \tag{3.3}$$

where $K_p = 0.1$ is the gain of the proportional controller (Fig. 3.3). It is set based on the maximum allowable variation in the battery SOC compared to SOC_{ref}. Since the value of P_{12} is restricted to the range between P_{12}^{-} and P_{12}^{+} (3.2), the value of $k(t)$ is between 0 and 1 (i.e., $0 \leq k(t) \leq 1$).

If the battery is depleting, the ARBS controller increases $P_{12}(t)$ thereby extending region 2 (engine) and reducing region 1 (motor) by an amount proportional to the difference between SOC_{ref} and $SOC(t)$. This process dynamically promotes the use of the engine and discourages the use of the battery thus protecting it from depletion.

The magnitude of the controller action depends on its gain K_p and the difference $(SOC(t) - SOC_{ref})$ (3.3). The limits on the value of $SOC(t)$ can be found using (3.3) and the constraints on $k(t)$.

$$SOC_{ref} - \frac{0.5}{K_p} \leq SOC(t) \leq SOC_{ref} + \frac{0.5}{K_p} \tag{3.4}$$

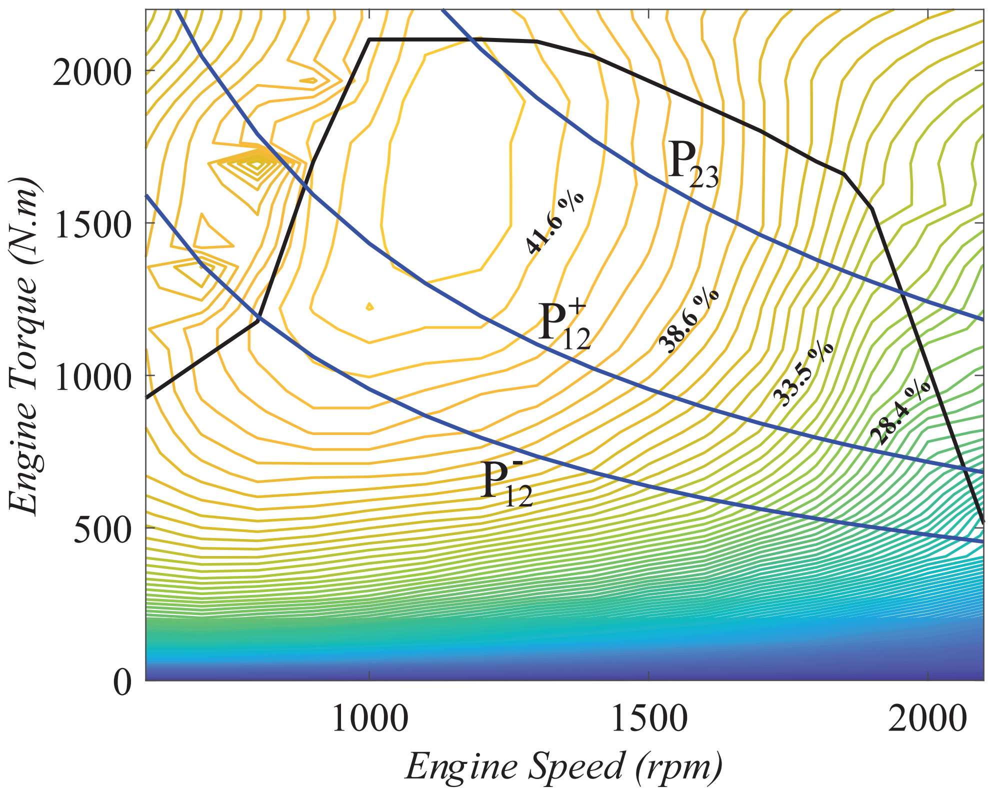

Fig. 3.4. Engine efficiency map with region boundaries for the ARBS strategy.

The limits on SOC(t) (3.4) depict the range of battery SOC during which the controller is active. Beyond these SOC values, the controller is saturated. According to (3.4), the value of K_p determines the range for which the controller would be in action. In this study, K_p is set to be 0.05, so that the controller is active when $SOC(t)$ is between 40% and 60%.

The proposed ARBS described above only modifies the boundary, $P_{12}(t)$, between regions 1 and 2 to a time variant boundary while keeping the boundary, P_{23}, between region 2 and 3 constant. It is possible to also apply a similar approach to P_{23}.

However P_{23} is already near the maximum torque curve as shown in Fig. 3.4. Therefore, increasing P_{23} will extend the engine region to include areas outside the allowable operating region of the engine. Reducing P_{23} will exclude areas where the engine is at its highest efficiency.

4. SIMULATION AND RESULT ANALYSIS

In order to implement the PRBS and proposed ARBS strategies, values for P_{23}, P_{12}, P_{12}^{-} and P_{12}^{+} are selected. P_{23} power level is fixed close to the maximum rated power of the engine whereas, the power level P_{12}^{+} is fixed close to the maximum rated power of the battery. The values of P_{12} for PRBS can be determined based on the engine efficiency map for best performance. Two simulations are performed in this study in order to compare ARBS and PRBS. The first (Section 4.1) evaluates both the strategies for short duty cycles of about 9.5 miles where the strategy parameters are set based on the engine efficiency maps. The short trips do not drain the batteries as much as the long trips. As a result, the short trip simulations evaluates both the strategies inside the SOC boundary conditions. The second (Section 4.2) compares the strategies over a long duty cycle for different values of P_{12} for PRBS and P_{12}^{-} for ARBS. The simulations with different values of P_{12} and P_{12}^{-} help study the effects of chosing these values on the HEV fuel economy. In long trip simulations, the SOC reaches it's minimum or maximum value more often than short trips. Thus the long trip simulations are affected by the SOC boundary conditions. The results of the two simulations are expressed in terms of miles per gallon equivalent (MPGe) metric to compare the two strategies. MPGe is a metric introduced by the EPA in 2011 [53] to compare vehicles with different energy sources. It represents the number of miles driven per diesel gallon equivalent energy and assumes that 1 gallon of diesel fuel has 38.08 kWh of energy [54]. The MPGe value is given by:

$$MPGe = \frac{D_m}{T_E} \cdot 38.08 \tag{4.1}$$

where D_m is the number of miles driven, and T_E is the total net energy spent over the trip in kWh. T_E is calculated by converting the change in SOC and the fuel spent by the vehicle to its energy content in kWh as follows:

$$T_E = F_C \cdot U_f - B_E \cdot (SOC(t_f) - SOC(t_0)) \tag{4.2}$$

where F_C is the actual fuel consumed in gallons, U_f is the energy content of one gallon of diesel fuel, B_E is the battery capacity, $SOC(t_f)$ is the final SOC and $SOC(t_0)$ is the initial SOC of the battery. The values of these parameters are maintained constant across all the simulations. It is worth noting that in the ECMS strategy, the equivalence factor is the weight assigned to the difference between SOC_{ref} and $SOC(t_0)$. This equivalence factor can take on different values and is adjusted according to the duty cycle. On the other hand, the B_E factor which is used to convert the change in SOC to the energy spent by the battery in the ARBS strategy is constant.

4.1 Short Trips Simulation

The HEV vehicle model described in chapter 2 is implemented with either the PRBS controller or the ARBS controller described in chapter 3. The resulting model was used to simulate the two strategies for 8 duty cycles. The values of the parameters used for the simulations are given in Table 4.1.

The value of P_{12} for PRBS and the value of P_{12}^{-} for ARBS is set 100 kW based on the engine efficiency map (Fig. 3.1). It can be seen in Fig. 3.1 that the engine operates in inefficient regions below the power level of 100 kW.

The 8 duty cycles are collected from a single heavy duty vehicle with 4 different drivers (Table 4.2). Each driver generated two duty cycles which include both city and highway traffic spanning varying distances. Drivers were instructed to exhibit good driving behavior in one of the duty cycle and bad driving behavior in the second duty cycle. Good behavior entails anticipating braking and coasting when possible.

Table 4.1.
Short trip simulation parameter values.

Parameters	Values
P_{12} (PRBS only)	100 kW
P_{12}^{+} (ARBS only)	150 kW
P_{12}^{-} (ARBS only)	100 kW
P_{23}	260 kW
P_m (PRBS only)	6 kW
SOC_{min}	35 %
SOC_{max}	65 %
SOC_m	5 %
SOC_{ref} (ARBS only)	50 %
P_{chg}	20 kW
K_p (ARBS only)	0.05
DPL	210 kW
CPL	-100 kW
Battery Size	11.31 kWh

The vehicle was driven on two routes around the Indianapolis area. Both routes have segments of city and highway driving.

Tables 4.3, 4.4 and 4.5 show the simulation results for different initial SOC values. The percent improvement (Imp) in $MPGe$ for the ARBS strategy compared to the PRBS strategy is calculated using (4.3) and shown in these tables for the 8 duty cycles.

$$Imp = \frac{MPGe_{ARBS} - MPGe_{PRBS}}{MPGe_{PRBS}} \cdot 100 \tag{4.3}$$

where $MPGe_{ARBS}$ and $MPGe_{PRBS}$ represent the miles per gallon equivalent for ARBS and PRBS, respectively.

Table 4.2.
Duty cycles characteristics.

Duty cycle	Driver	Distance (miles)	Behavior	Route
1	1	7.89	good	A
2	1	9.61	bad	A
3	2	9.69	good	A
4	2	9.78	bad	A
5	3	9.56	good	A
6	3	9.57	bad	A
7	4	7.56	good	B
8	4	7.57	bad	B

The average Imp across the 8 duty cycles in Tables 4.3, 4.4 and 4.5 for different initial $SOCs$ are 0.16%, 0.09% and 1.19%, respectively. These results indicate that, in general, the performance enhancement due to the ARBS strategy is very small for low $SOC(t_0)$ values (i.e., $\leq$ 50%). The performance of ARBS increases when $SOC(t_0)$ is 63%.

The different $SOC(t_0)$ values simulated in the three tables can be considered as sample intermediate values of battery SOC during an extended duty cycle. During this extended cycle, instances of high $SOC(t)$ at the beginning of a road segment will lead to a higher Imp when the ARBS strategy is used compared to the PRBS strategy. Whereas for instances of low $SOC(t)$ at the beginning of a road segment, the ARBS and PRBS strategies will have similar performances. Instances of high $SOC(t)$ occur, for example, when there are opportunities for regenerative braking in the duty cycle. For these cases ARBS is expected to show improved fuel consumption.

Fig. 4.1 shows the vehicle speed for duty cycles 3 and 5. These two duty cycles are generated from good driving behavior by two different drivers. Duty cycle 3 has

Table 4.3.
Fuel consumption for the 8 duty cycles resulting from the PRBS and ARBS energy management strategies for an initial SOC of 37%.

	Strategy	Actual Fuel Consumed F_C, (gallons)	Final SOC $SOC(t)$, (%)	Total Net Energy T_E, (kWh)	MPGe (miles per 33.7 kWh)	Percent Improvement Imp, (%)
1	PRBS	1.58	41.22	57.98	4.59	1.82
	ARBS	1.54	38.62	56.95	4.67	
2	PRBS	1.83	36.34	67.70	4.79	-0.03
	ARBS	1.83	36.75	67.73	4.78	
3	PRBS	1.52	37.00	56.35	5.80	-0.14
	ARBS	1.52	36.77	56.43	5.79	
4	PRBS	2.24	37.80	82.73	3.99	0.25
	ARBS	2.22	35.21	82.53	4.00	
5	PRBS	1.60	36.83	59.15	5.45	0.23
	ARBS	1.60	37.62	59.00	5.46	
6	PRBS	1.96	37.15	72.33	4.46	-0.99
	ARBS	1.98	37.26	73.06	4.42	
7	PRBS	1.02	35.71	38.06	6.69	0.03
	ARBS	1.03	35.95	38.05	6.70	
8	PRBS	1.05	38.68	38.78	6.58	0.17
	ARBS	1.05	38.78	38.71	6.59	
	Average					0.16

more highway coasting whereas duty cycle 5 is more urban. In order to compare the two EMS strategies, the engine operating points for duty cycles 3 and 5 are shown in Fig. 4.2 and Fig. 4.3, respectively. The circles in these figures represent the power delivered by the engine, sampled at 1 second intervals during the trip.

For PRBS, the engine region is between $P_{12,PRBS}$ and P_{23}, whereas for the ARBS strategy the engine region is between $P_{12}(t)$ and P_{23}. $P_{12}(t)$ is greater than P_{12}^{-} as long as $SOC(t)$ is greater than SOC_{ref} and the engine operates at a high efficiency under this condition. Moreover, the motor region for the ARBS strategy is wider than that of PRBS since $P_{12}(t)$ varies between P_{12}^{-} and P_{12}^{+} during the duty cycle.

Table 4.4.
Fuel consumption for the 8 duty cycles resulting from the PRBS and ARBS energy management strategies for an initial SOC of 50%.

	Strategy	Actual Fuel Consumed F_C, (gallons)	Final SOC $SOC(t)$, (%)	Total Net Energy T_E, (kWh)	MPGe (miles per 33.7 kWh)	Percent Improvement Imp, (%)
1	PRBS	1.51	46.87	56.17	4.74	-0.20
	ARBS	1.51	46.27	56.29	4.73	
2	PRBS	1.69	37.05	64.15	5.05	0.68
	ARBS	1.68	36.54	63.72	5.09	
3	PRBS	1.40	37.12	53.31	6.13	0.63
	ARBS	1.39	37.24	52.98	6.17	
4	PRBS	2.08	35.31	78.64	4.19	-0.32
	ARBS	2.09	36.49	78.90	4.18	
5	PRBS	1.45	36.27	55.23	5.83	-0.82
	ARBS	1.47	37.44	55.69	5.79	
6	PRBS	1.83	36.62	69.27	4.66	0.34
	ARBS	1.83	36.92	69.05	4.67	
7	PRBS	0.90	35.86	35.00	7.29	0.30
	ARBS	0.90	36.11	34.90	7.31	
8	PRBS	0.93	38.66	35.67	7.15	0.11
	ARBS	0.93	40.08	35.64	7.16	
	Average					0.09

When comparing the two duty cycles, higher power demands are observed for duty cycle 5 because of its urban characteristic. In addition, the motor only mode is less frequent in this duty cycle and there are more opportunities for regenerative braking. These factors help sustain the battery SOC above SOC_{min}. Therefore, the ARBS operates the engine in higher efficiency region compared to the PRBS strategy for duty cycle 5 as shown by the fewer number of operating points below P_{12}^{+} in Fig. 4.3 for ARBS compared to the PRBS strategy.

The impact of coasting can also be observed by comparing Figures 4.2 and 4.3. A smaller amount of power is required during highway coasting, a characteristic of duty cycle 3. Indeed, less acceleration events are observed during coasting (duty cycle 3)

Table 4.5.
Fuel consumption for the 8 duty cycles resulting from the PRBS and ARBS energy management strategies for an initial SOC of 63%.

	Strategy	Actual Fuel Consumed F_C, (gallons)	Final SOC $SOC(t)$, (%)	Total Net Energy T_E, (kWh)	MPGe (miles per 33.7 kWh)	Percent Improvement Imp, (%)
1	PRBS	1.51	59.48	56.25	4.73	2.74
	ARBS	1.44	50.13	54.75	4.86	
2	PRBS	1.63	43.82	62.36	5.20	0.44
	ARBS	1.61	41.57	62.09	5.22	
3	PRBS	1.27	37.11	49.80	6.56	-0.39
	ARBS	1.27	36.90	50.00	6.54	
4	PRBS	1.97	39.30	75.50	4.37	0.05
	ARBS	1.96	37.74	75.48	4.37	
5	PRBS	1.45	48.07	55.35	5.82	2.76
	ARBS	1.38	39.63	53.86	5.98	
6	PRBS	1.74	40.05	66.84	4.83	1.48
	ARBS	1.70	36.64	65.86	4.90	
7	PRBS	0.82	37.80	33.06	7.72	0.44
	ARBS	0.81	36.90	32.92	7.75	
8	PRBS	0.81	38.98	32.64	7.82	2.04
	ARBS	0.78	36.51	31.99	7.98	
	Average					1.19

compared to an urban duty cycle (duty cycle 5). As a result, fewer operating points lie on the P_{23} boundary in Fig. 4.2 compared to Fig. 4.3.

There are few engine operating points in the low efficiency region for duty cycle 3 under the ARBS strategy (Fig. 4.2). This can be explained by the fact that the battery depletes quicker under ARBS compared to PRBS for this duty cycle. Once the battery $SOC(t)$ reaches SOC_{min}, the engine starts operating in low efficiency regions.

The improvement in fuel consumption obtained for duty cycle 5 under ARBS is due to the regenerative braking opportunities present in urban and stop-and-do duty cycles that can help maintain high levels of SOCs for the battery.

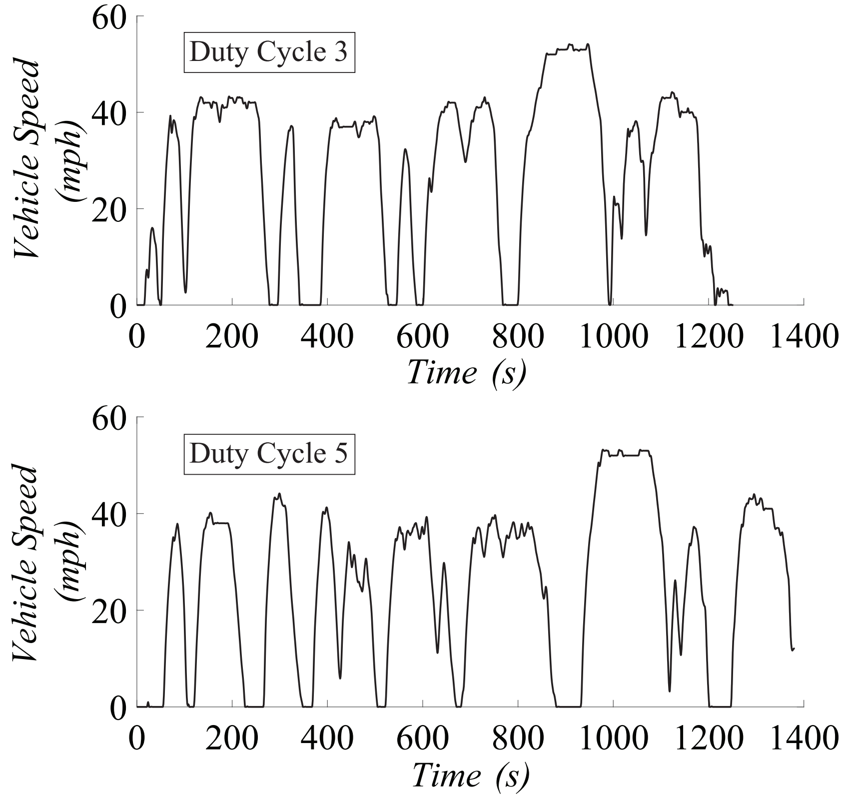

Fig. 4.1. Vehicle speed for duty cycles 3 and 5.

Varying the parameters of the PRBS strategy while maintaining the ARBS parameters unchanged has an impact on the MPGe improvement due to the ARBS strategy for each duty cycle. Table 4.6 shows the average improvement values for the 8 duty cycles corresponding to different values of P_{12}. These results indicate that while the percent improvement varies, it still favors ARBS. The SOC_{min} value for the PRBS strategy was also changed to 50% from 35% in an attempt, as in the case of ARBS, to maintain the battery SOC above 50% (i.e., the value of SOC_{ref} in ARBS). This change had a negative impact on PRBS as it reduced the operating range of the battery and resulted in an average Imp of 7.49% for ARBS over the 8 duty cycles.

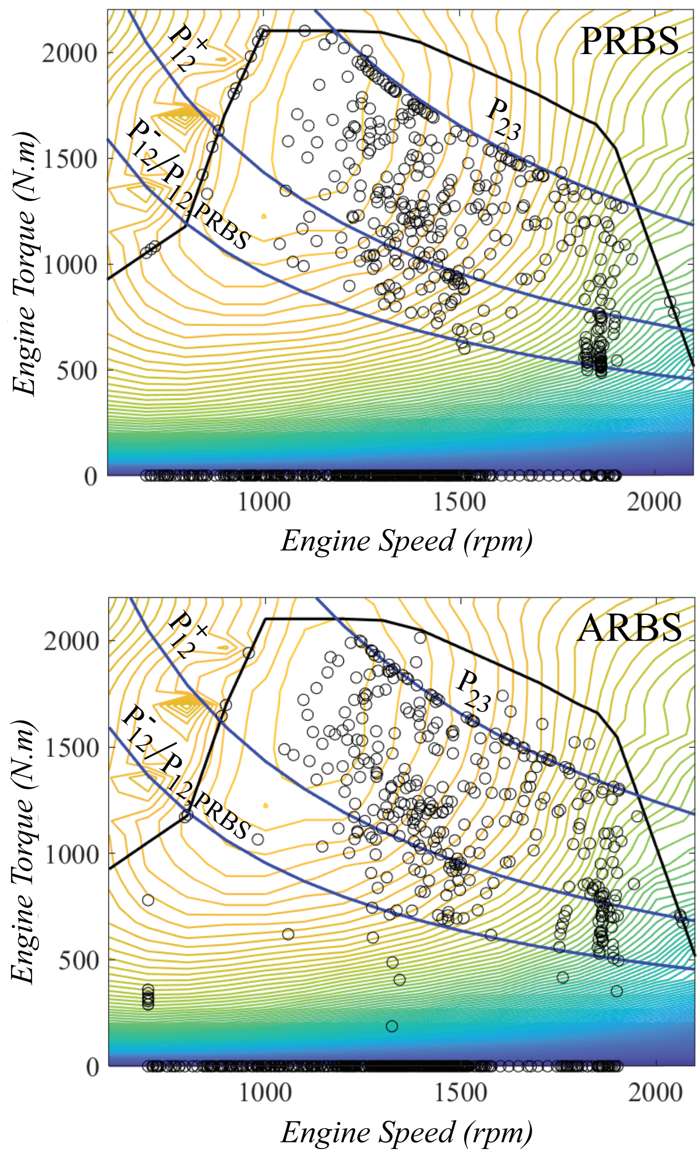

Fig. 4.2. Engine operating points for duty cycle 3 under PRBS and ARBS for $SOC(t_0) = 63\%$.

4.2 Long Trip Simulation

While hybridizing a conventional vehicle (aftermarket hybridization), the engine's efficiency maps are usually unknown. It is thus difficult to select appropriate values for P_{12} in PRBS P_{12}^{-} in ARBS that are necessary to configure the vehicle. In order

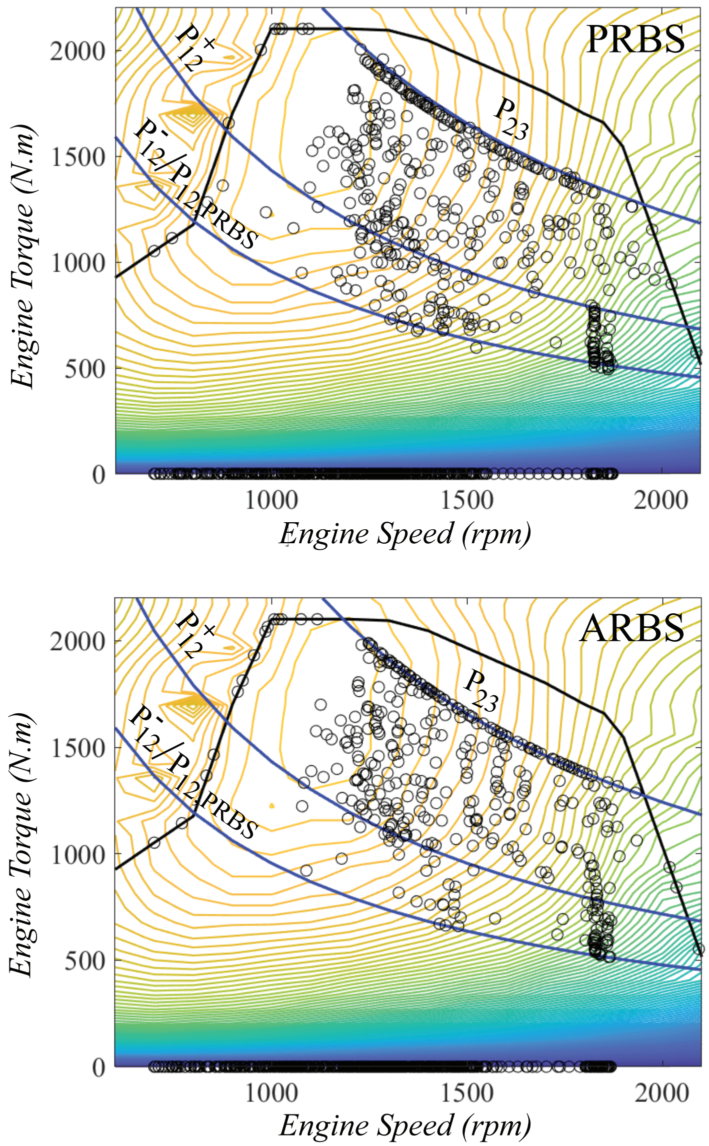

Fig. 4.3. Engine operating points for duty cycle 5 under PRBS and ARBS for $SOC(t_0) = 63\%$.

to compare the two strategies, the HEV model was simulated with different values of P_{12} and P_{12}^{-}. The values of parameters used in this simulation are given in Table 4.7. This simulation was performed on a long duty cycle constructed from 6 of the 8 short duty cycles mentioned in Section 4.1. This long duty cycle is about 56 miles long and operates for about 8000 s.

Table 4.6.
Average improvement in total equivalent fuel economy over the 8 duty cycles for different values of P_{12} in the PRBS strategy.

P_{12}, PRBS (kW)	Average Imp (%)
80	2.46
110	0.41
140	2.23

Table 4.7.
Parameter values for long trip simulation with 365V battery system.

Parameters	Values
P_{12} (PRBS only)	0 to 140 kW
P_{12}^{+} (ARBS only)	150 kW
P_{12}^{-} (ARBS only)	0 to 140 kW
P_{23}	260 kW
P_m (PRBS only)	6 kW
SOC_{min}	35 %
SOC_{max}	65 %
SOC_m	5 %
SOC_{ref} (ARBS only)	50 %
P_{chg}	20 kW
K_p (ARBS only)	0.05
DPL	210 kW
CPL	-100 kW
Battery Size	11.31 kWh
Battery Nominal Voltage	365 V

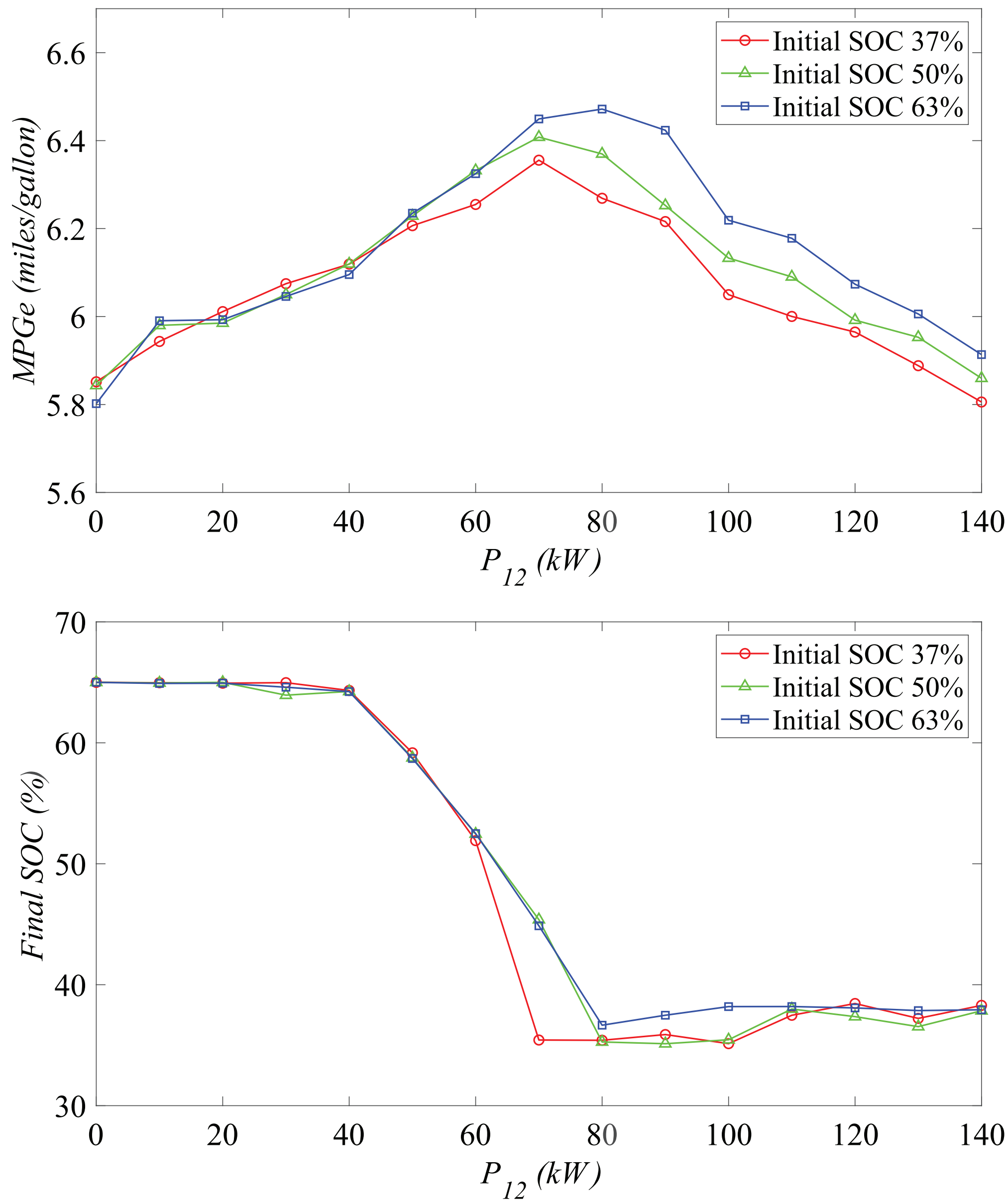

Fig. 4.4. (a) MPGe (b) Battery Final SOC for different values of P_{12} in the PRBS strategy.

Fig. 4.4 and 4.5 show the simulation results for three different values of initial SOC. In Fig. 4.4 the long duty cycle was simulated with the PRBS strategy for 15 different values of P_{12} ranging from 0 kW to 140 kW with incremental steps of 10 kW.

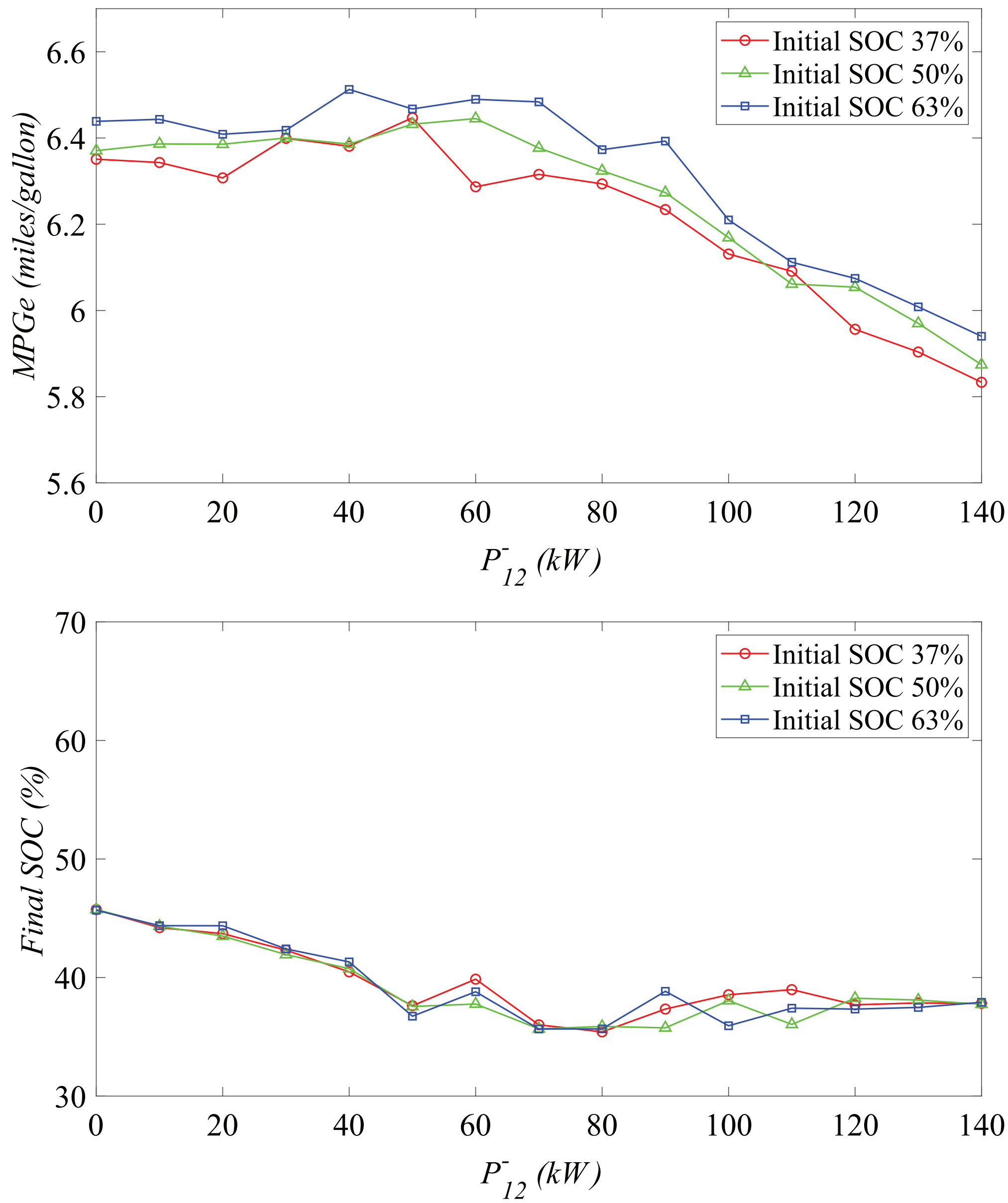

Fig. 4.5. (a) MPGe (b) Battery Final SOC for different values of P_{12}^{-} in the ARBS strategy.

In Fig. 4.5, the same duty cycle was simulated with the ARBS strategy for different values of P_{12}^{-} also ranging from 0 kW to 140 kW with incremental steps of 10 kW.

The MPGe value for PRBS is highest when P_{12} is around 75 kW. The MPGe is low when P_{12} is low because the engine region is large and extends to its inefficient regions. Moreover, the battery is not discharged much when P_{12} is low because the motor region is small causing the battery to only charge through regenerative braking. As a result the battery final SOC is high for low values of P_{12} as seen in Fig 4.4b. When P_{12} is high, the motor region is large causing the battery to drain faster and making it unusable during the vehicle operation. At the same time the engine operates in its inefficient regions decreasing the vehicle MPGe. Fig 4.4b shows that for higher values of P_{12}, the final SOC is close to its lower limit of 35%. In fact, high MPGe (i.e., around 6.4 miles/gallon) are only possible for a very narrow range of P_{12} values.

In contrast, for ARBS, and as shown in Fig 4.5a, the MPGe value is maintained at a high value (i.e., around 6.4 miles/gallon) for an extended range of P_{12}^{-} values ranging from 0 kW to 70 kW. The MPGe value is high for low values of P_{12}^{-} because the ARBS controller can adjust the value of $P_{12}(t)$ in order to keep the battery SOC is kept around the reference SOC of 50%. It neither completely drains the battery nor charges it to the upper limit (65%) keeping the battery available to charge and discharge throughout the duty cycle operation and thus avoids the inefficient engine regions. Fig. 4.5b shows that the battery final SOC is maintained around 50% for low values of P_{12}^{-}. As P_{12}^{-} increases, the $P_{12}(t)$ value which is constrained by P_{12}^{-} and P_{12}^{+}, also increases resulting in a similar scenario as in the case of PRBS with high P_{12}. Therefore, the MPGe decreases for high values of P_{12}^{-}. The described behavior of MPGe under the ARBS strategy makes the selection of optimal configuration parameters easier than in the case of the PRBS strategy.

Fig 4.6a shows the long duty cycle used in this simulation and Fig 4.6b shows the battery SOC during the vehicle operation for both strategies with $P_{12} = 20$ kW for PRBS and $P_{12}^{-} = 20$ kW for ARBS. The value of $P_{12}(t)$, in the ARBS controller, is depicted in Fig 4.6c. The initial battery SOC is kept at 50% for these simulations. The battery SOC increases for PRBS strategy because of the low value of P_{12}, whereas the ARBS controller tries to maintain the battery SOC around 50% (Fig 4.6b) by adjusting the value of $P_{12}(t)$ (Fig 4.6c). As the battery SOC decreases below 50%, the ARBS controller tries to preserve the SOC by lowering the $P_{12}(t)$ power level and

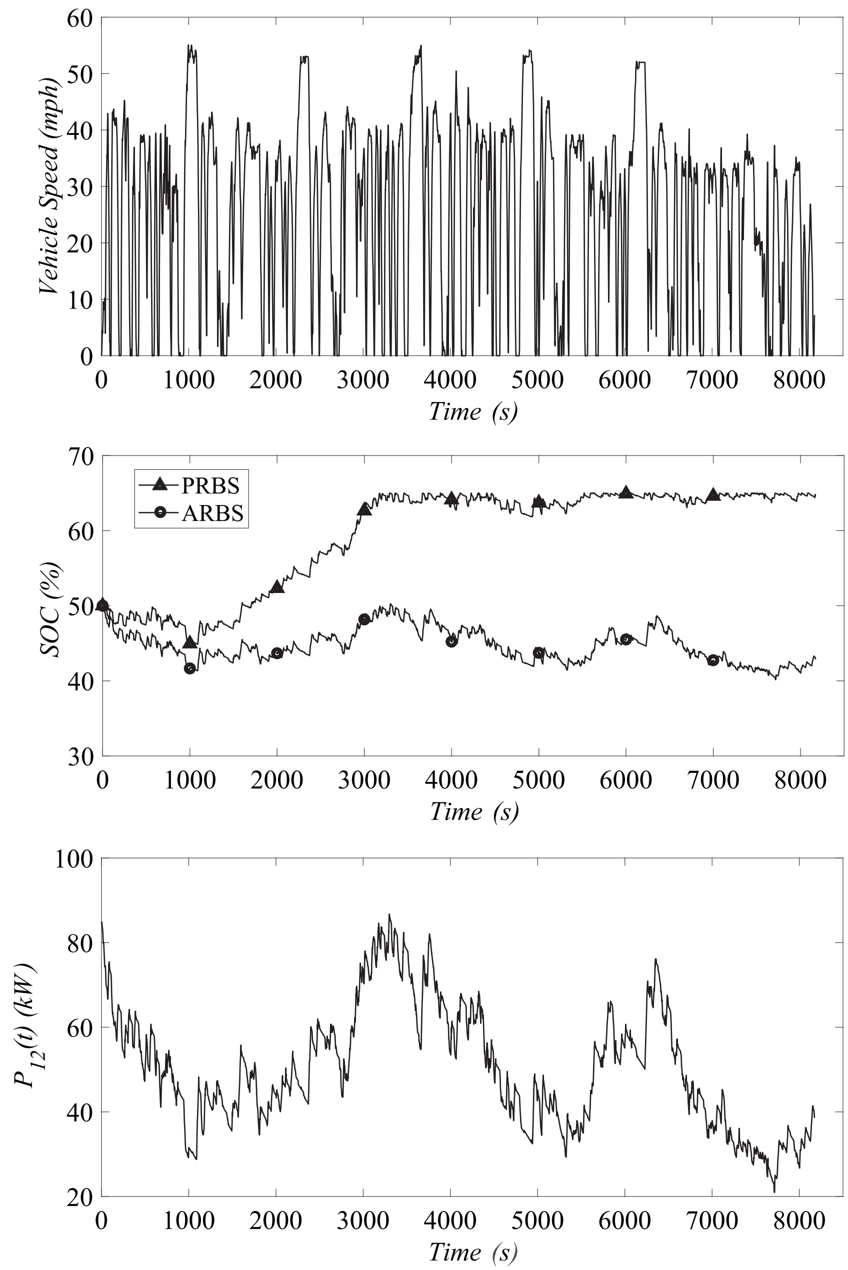

Fig. 4.6. (a) Vehicle Speed (b) Battery SOC (c) $P_{12}(t)$ for long duty cycle operation.

equivalently reducing the motor region. Conversely, the ARBS controller increases the value $P_{12}(t)$ when the SOC increases beyond 50%. This action of the controller reduces the engine inefficient operating points compared to the PRBS strategy and

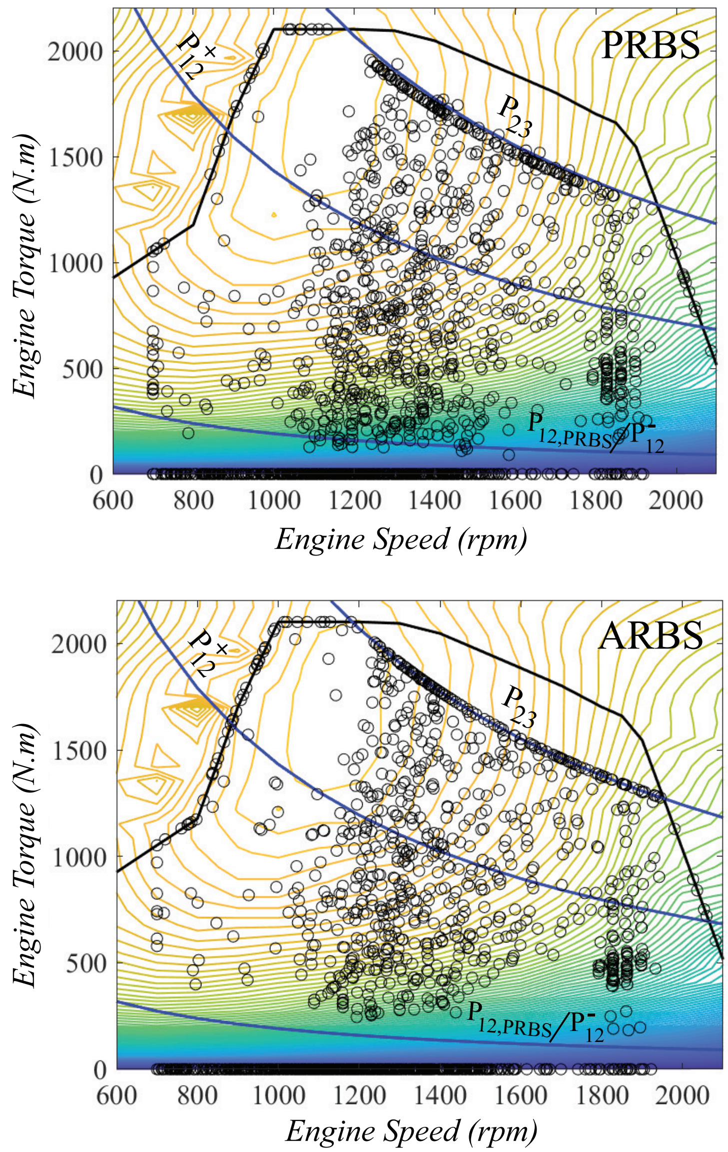

Fig. 4.7. PRBS and ARBS Engine Operating points for $P_{12} = 20kW$ (PRBS) and $P_{12}^{-} = 20kW$ (ARBS).

also keeps the SOC around 50%. Fig 4.7 shows the engine operating points at an interval of 4 s during the long duty cycle operation for both the strategies. This figure illustrates that the engine is operated in inefficient regions more frequently in PRBS than in the ARBS. The engine has more operating points near the $P_{12,ARBS}$ curve during PRBS strategy than during the ARBS strategy.

Table 4.8.
Short trip simulation parameter values.

Parameters	Values
P_{12} (PRBS only)	0 to 27.5 kW
P_{12}^{+} (ARBS only)	30 kW
P_{12}^{-} (ARBS only)	0 to 27.5 kW
P_{23}	260 kW
P_m (PRBS only)	3 kW
SOC_{min}	35 %
SOC_{max}	65 %
SOC_m	5 %
SOC_{ref} (ARBS only)	50 %
P_{chg}	10 kW
K_p (ARBS only)	0.05
DPL	30 kW
CPL	-30 kW
Battery Size	2.82 kWh
Battery Nominal Voltage	48 V

In order to compare the benefits of ARBS over PRBS in the 48V full hybrid system, the HEV model battery was modified with a 48V battery system with a peak power delivery of 30 kW. The weight of the vehicle was also changed from 25000 kg to 7000 kg so that the 48V systems are able to propel the vehicle in electric-only mode. The parameters used for this simulation are given in Table 4.8. The same long duty cycle that was used in the previous simulation is used here. The values of P_{12} and P_{12}^{-} are varied from 0 to 27.5 kW with incremental steps of 2.5 kW. The simulation helps to study effects of selecting different values of P_{12} and P_{12}^{-} in a 48V battery system.

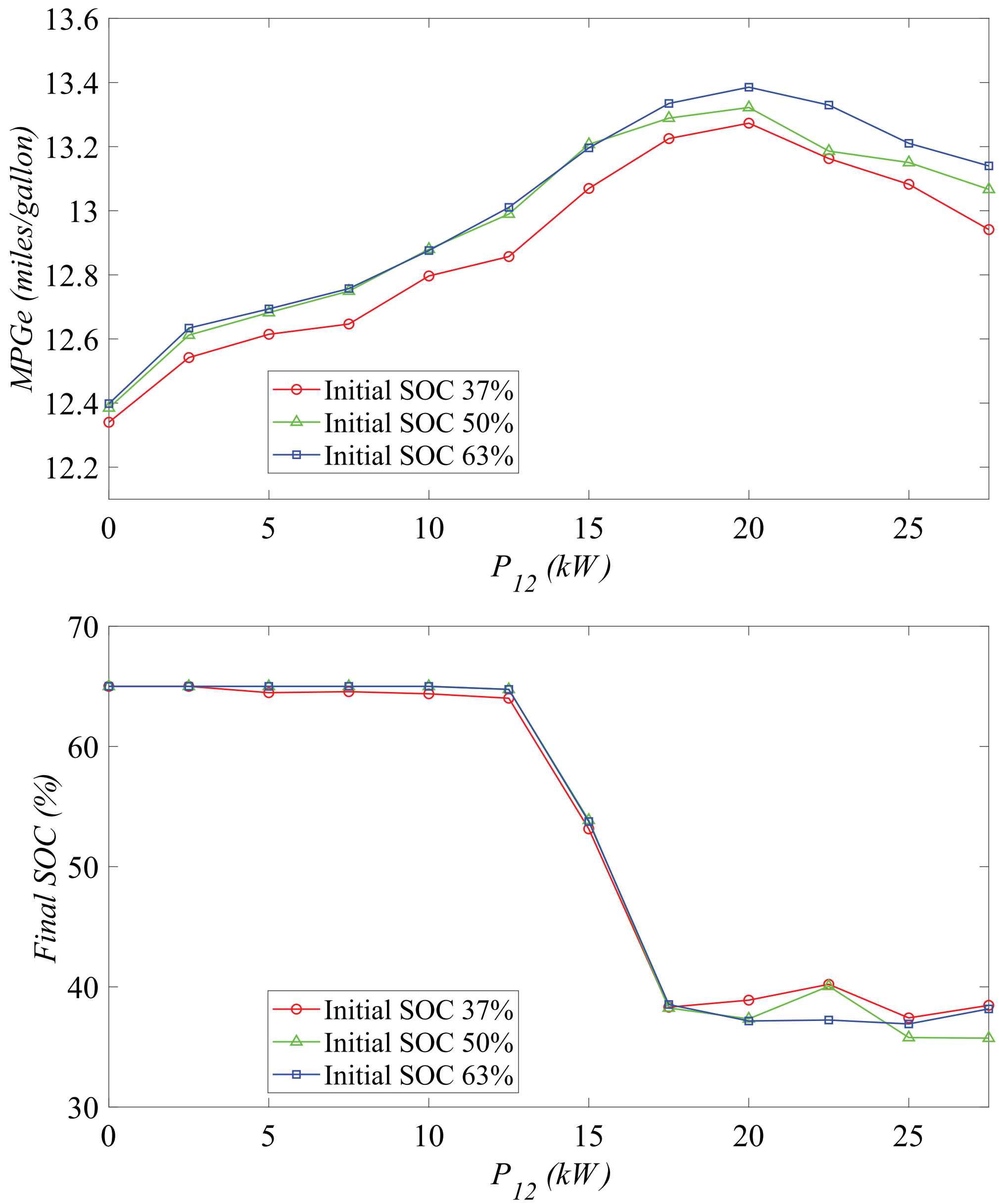

Fig. 4.8. (a) MPGe (b) Battery Final SOC for different values of P_{12} in the PRBS strategy.

A similar MPGe and SOC behavior is observed for 48V hybrid systems when compared to the previous 365V system. The MPGe value for ARBS strategy is high around 13.4 miles/gallon for P_{12}^{-} values ranging from 0 to 15 kW as seen in Fig. 4.9. Whereas, the MPGe reaches its highest point of 13.3 miles/gallon at $P_{12} = 20$ kW

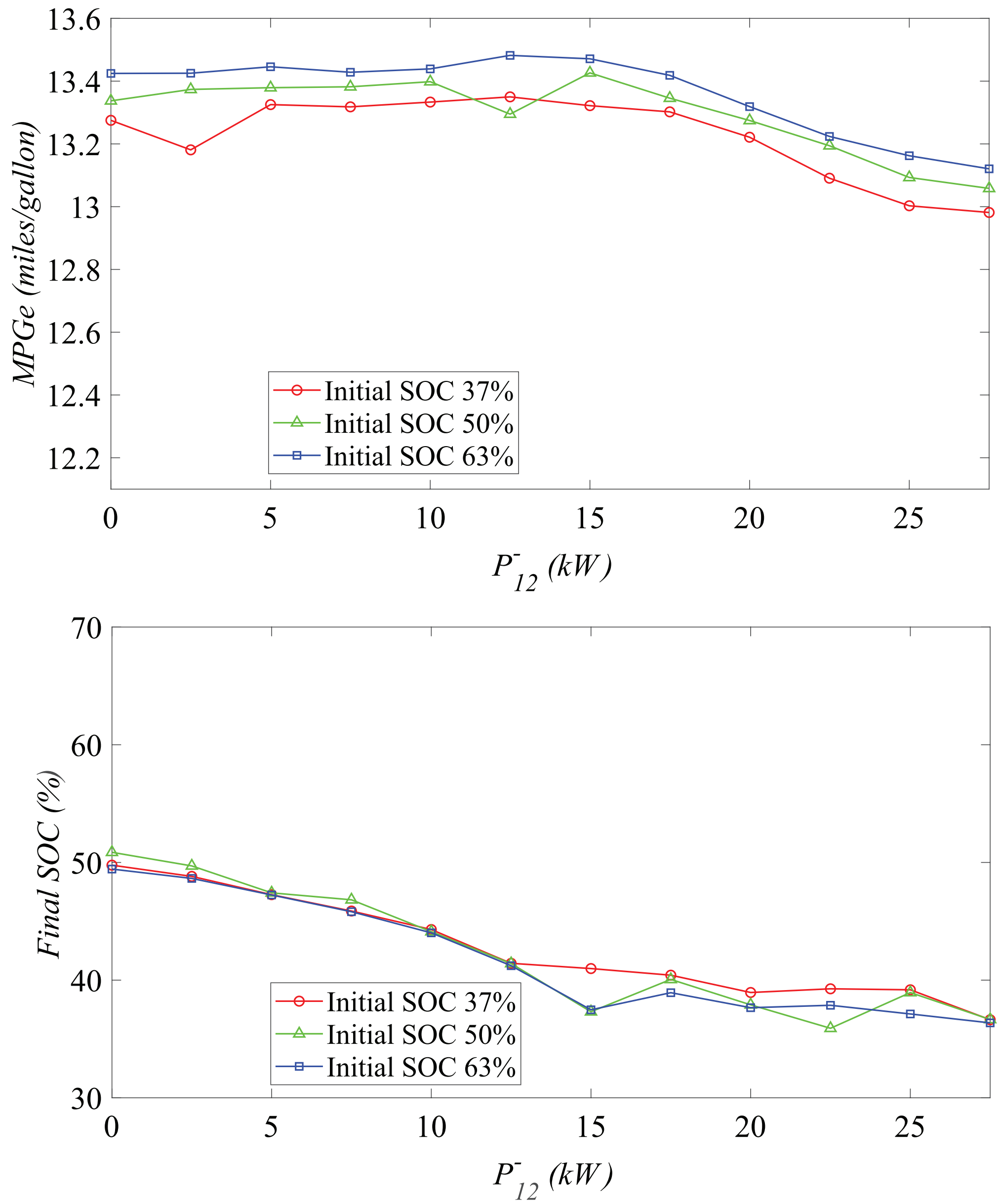

Fig. 4.9. (a) MPGe (b) Battery Final SOC for different values of P_{12}^{-} in the ARBS strategy.

for PRBS strategy. The ARBS strategy also maintains the battery SOC within the 40% to 60% range for P_{12}^{-} values ranging from 0 to 12.5 kW. As seen from the results in Fig. 4.9, the ARBS strategy is able to maintain a high MPGe when the battery final SOC is around its reference value and as the final SOC reduces close to its lower limit, the MPGe value starts decreasing. The availability of the battery during the operation of ARBS helps it to optimize the fuel consumption.

Thus, the ARBS strategy can be tuned easily than the PRBS for both the hybrid systems (i.e., 365V and 48V). In addition, the ARBS performs the best when $P_{12}^{-} = 0$ kW by maintaining the highest final SOC in comparison to all the other values of P_{12}^{-} for both the hybrid systems.

5. CONCLUSION

This thesis introduces an adaptive EMS strategy for a parallel HEV and compares it with the state-of-the-art PRBS strategy. The increase in the equivalent fuel economy exhibited by the ARBS strategy varies depending on the duty cycle and the initial SOC for short trips. For $SOC(t_0) = 63\%$, an average improvement of 1.19% across 8 short duty cycles was obtained. The highest level of improvement in MPGe (i.e., 2.76%) was obtained for duty cycle 5. Typically, this level of improvement is expected for extended duty cycles with frequent opportunities for regenerative braking. Given that the ARBS controller is a simple linear controller that is added in front of the PRBS controller, this increase in performance does not incur any significant increase in computational cost.

The results in Section 4.2 demonstrate that ARBS can be used effectively to support the hybridization of conventional vehicles with 48V full hybrid systems where typically the engine efficiency maps are unknown and a simple online strategy is needed. Both the PRBS and ARBS strategies are easy to implement. However, the ARBS is easier to configure compared to the PRBS. Indeed, instead of attempting to estimate the appropriate value of P_{12} as in the case of PRBS, the value of P_{12}^{-} in ARBS can be set to 0 kW. The ARBS will then automatically adjust the dynamic value of $P_{12}(t)$ in order to achieve high MPGe. The ARBS strategy also maintains the SOC around its reference value when P_{12}^{-} is set to 0 kW.

Future work will investigate into dynamic variation of P_{23} value along with P_{12}. Faster and more control can be achieved by varying both the values simultaneously. Instead of constant power lines defining the operating region boundaries for the engine and the motor, a more complex shaped boundary (like elliptical) can be considered.

REFERENCES

REFERENCES

[1] hybridCARS.com, "History of hybrid vehicles," https://web.archive.org/web/20090904154040/www.hybridcars.com/history/history-of-hybrid-vehicles, March 27,2006 (accessed August 26, 2019).

[2] J. M. Ogden, M. M. Steinbugler, and T. G. Kreutz, "A comparison of hydrogen, methanol and gasoline as fuels for fuel cell vehicles: implications for vehicle design and infrastructure development," *Journal of power sources*, vol. 79, no. 2, pp. 143–168, 1999.

[3] C. Thomas, "Fuel cell and battery electric vehicles compared," *international journal of hydrogen energy*, vol. 34, no. 15, pp. 6005–6020, 2009.

[4] www.fueleconomy.gov, *Where Energy Goes: Electric Cars*, (accessed September 1, 2019). [Online]. Available: https://www.fueleconomy.gov/feg/atv-ev.shtml

[5] F. Schlachter, "The back page - has the battery bubble burst?" *American Physical Society (APS) News*, vol. 21, no. 8, p. 8, 2012.

[6] K. Ç. Bayindir, M. A. Gözüküçük, and A. Teke, "A comprehensive overview of hybrid electric vehicle: Powertrain configurations, powertrain control techniques and electronic control units," *Energy conversion and Management*, vol. 52, no. 2, pp. 1305–1313, 2011.

[7] S. Kowalec, *12V / 48V Hybrid Vehicle Technology*, (accessed September 1, 2019). [Online]. Available: https://www.psma.com/sites/default/files/uploads/tech-forums-transportation-power-electronics/presentations/is115-12v-48v-hybrid-vehicle-technology.pdf

[8] A. Ziebinski, R. Cupek, H. Erdogan, and S. Waechter, "A survey of adas technologies for the future perspective of sensor fusion," in *International Conference on Computational Collective Intelligence.* Springer, 2016, pp. 135–146.

[9] R. Jurgen, *V2V/V2I communications for improved road safety and efficiency.* SAE, 2012.

[10] P. Zhang, F. Yan, and C. Du, "A comprehensive analysis of energy management strategies for hybrid electric vehicles based on bibliometrics," *Renewable and Sustainable Energy Reviews*, vol. 48, pp. 88–104, 2015.

[11] D. Bianchi, L. Rolando, L. Serrao, S. Onori, G. Rizzoni, N. Al-Khayat, T.-M. Hsieh, and P. Kang, "A rule-based strategy for a series/parallel hybrid electric vehicle: an approach based on dynamic programming," in *ASME 2010 Dynamic Systems and Control Conference.* American Society of Mechanical Engineers, 2010, pp. 507–514.

[12] J. Wu, C.-H. Zhang, and N.-X. Cui, "Pso algorithm-based parameter optimization for hev powertrain and its control strategy," *International Journal of Automotive Technology*, vol. 9, no. 1, pp. 53–59, 2008.

[13] S. Onori, L. Serrao, and G. Rizzoni, *Hybrid electric vehicles: Energy management strategies*. Springer, 2016.

[14] C. Sun, H. He, and F. Sun, "The role of velocity forecasting in adaptive-ecms for hybrid electric vehicles," *Energy Procedia*, vol. 75, pp. 1907–1912, 2015.

[15] C.-C. Lin, H. Peng, J. W. Grizzle, and J.-M. Kang, "Power management strategy for a parallel hybrid electric truck," *IEEE transactions on control systems technology*, vol. 11, no. 6, pp. 839–849, 2003.

[16] H. Banvait, S. Anwar, and Y. Chen, "A rule-based energy management strategy for plug-in hybrid electric vehicle (phev)," in *American Control Conference, 2009. ACC'09.* IEEE, 2009, pp. 3938–3943.

[17] N. J. Schouten, M. A. Salman, and N. A. Kheir, "Fuzzy logic control for parallel hybrid vehicles," *IEEE transactions on control systems technology*, vol. 10, no. 3, pp. 460–468, 2002.

[18] X. Huang, Y. Tan, and X. He, "An intelligent multifeature statistical approach for the discrimination of driving conditions of a hybrid electric vehicle," *IEEE Transactions on Intelligent Transportation Systems*, vol. 12, no. 2, pp. 453–465, 2011.

[19] Z. Chen, C. C. Mi, J. Xu, X. Gong, and C. You, "Energy management for a power-split plug-in hybrid electric vehicle based on dynamic programming and neural networks," *IEEE Transactions on Vehicular Technology*, vol. 63, no. 4, pp. 1567–1580, 2014.

[20] C. Mansour and D. Clodic, "Dynamic modeling of the electro-mechanical configuration of the toyota hybrid system series/parallel power train," *International Journal of Automotive Technology*, vol. 13, no. 1, p. 143, 2012.

[21] G. E. Box and N. R. Draper, *Empirical model-building and response surfaces.* John Wiley & Sons, 1987.

[22] H. Barths, C. Hasse, and N. Peters, "Computational fluid dynamics modelling of non-premixed combustion in direct injection diesel engines," *International Journal of Engine Research*, vol. 1, no. 3, pp. 249–267, 2000.

[23] C. Mei, "On teaching the simplification of block diagrams," *International Journal of Engineering Education*, vol. 18, no. 6, pp. 697–703, 2002.

[24] A. H. Zaabab, Q.-J. Zhang, and M. Nakhla, "A neural network modeling approach to circuit optimization and statistical design," *IEEE Transactions on Microwave Theory and Techniques*, vol. 43, no. 6, pp. 1349–1358, 1995.

[25] L. Ljung, *System identification: theory for the user.* Prentice-hall, 1987.

[26] K. Han, M. Choi, B. Lee, and S. B. Choi, "Development of a traction control system using a special type of sliding mode controller for hybrid 4wd vehicles," *IEEE Transactions on Vehicular Technology*, vol. 67, no. 1, pp. 264–274, 2018.

[27] Z. Zhang, K. Chau, and Z. Wang, "Analysis and stabilization of chaos in the electric-vehicle steering system," *IEEE Transactions on Vehicular Technology*, vol. 62, no. 1, pp. 118–126, 2013.

[28] Y. Ko, J. Lee, and H. Lee, "A supervisory control algorithm for a series hybrid vehicle with multiple energy sources," *IEEE Transactions on Vehicular Technology*, vol. 64, no. 11, pp. 4942–4953, 2015.

[29] V. Ngo, T. Hofman, M. Steinbuch, A. Serrarens *et al.*, "Optimal control of the gearshift command for hybrid electric vehicles," *IEEE Transactions on Vehicular Technology*, vol. 61, no. 8, p. 3531, 2012.

[30] L. Wang, E. G. Collins, and H. Li, "Optimal design and real-time control for energy management in electric vehicles," *IEEE Transactions on Vehicular Technology*, vol. 60, no. 4, pp. 1419–1429, 2011.

[31] W. Nie, V. C. Lee, D. Niyato, Y. Duan, K. Liu, and S. Nutanong, "A quality-oriented data collection scheme in vehicular sensor networks," *IEEE Transactions on Vehicular Technology*, 2018.

[32] U. Lee, E. Magistretti, M. Gerla, P. Bellavista, and A. Corradi, "Dissemination and harvesting of urban data using vehicular sensing platforms," *IEEE transactions on vehicular technology*, vol. 58, no. 2, pp. 882–901, 2009.

[33] Z. Ben Miled and M. O. French, "Towards a reasoning framework for digital clones using the digital thread," in *55th AIAA Aerospace Sciences Meeting*, 2017, p. 0873.

[34] *GTPower Software*, (Accessed: December 12, 2017). [Online]. Available: http://www.gtisoft.com

[35] U. Renberg, "1d engine simulation of a turbocharged si engine with cfd computation on components," Ph.D. dissertation, KTH Royal Institute of Technology, Stockholm, 2008.

[36] R. Sharma, D. Nesic, and C. Manzie, "Model reduction of turbocharged (tc) spark ignition (si) engines," *IEEE Transactions on Control Systems Technology*, vol. 19, no. 2, pp. 297–310, 2011.

[37] R. Lygoe, "Fitting automotive microprocessor control look-up tables to a response surface model using optimisation methods," SAE Technical Paper, Tech. Rep., 1998.

[38] T. L. Fine, *Feedforward neural network methodology.* Springer Science & Business Media, 2006.

[39] R. Lygoe, "Fitting automotive microprocessor control look-up tables to a response surface model using optimisation methods," SAE Technical Paper, Tech. Rep., 1998.

[40] T. Markel, A. Brooker, T. Hendricks, V. Johnson, K. Kelly, B. Kramer, M. OKeefe, S. Sprik, and K. Wipke, "Advisor: a systems analysis tool for advanced vehicle modeling," *Journal of power sources*, vol. 110, no. 2, pp. 255–266, 2002.

[41] D. Ngo, "Gear shift strategies for automotive transmissions," Ph.D. dissertation, Technische Universiteit Eindhoven, 2012.

[42] T. D. Gillespie, "Fundamentals of vehicle dynamics. 1992," *Warrendale, PA: Society of Automotive Engineers*, vol. 519.

[43] A. Swift, "Calculation of vehicle aerodynamic drag coefficients from velocity fitting of coastdown data," *Journal of Wind Engineering and Industrial Aerodynamics*, vol. 37, no. 2, pp. 167–185, 1991.

[44] B. P. Wiegand, "Estimation of the rolling resistance of tires," SAE Technical Paper, Tech. Rep., 2016.

[45] S. Pickenhain and A. Burtchen, "Optimal energy control of hybrid vehicles," in *Modeling, Simulation and Optimization of Complex Processes HPSC 2015*. Springer, 2017, pp. 179–188.

[46] T. Huria, M. Ceraolo, J. Gazzarri, and R. Jackey, "High fidelity electrical model with thermal dependence for characterization and simulation of high power lithium battery cells," in *2012 IEEE International Electric Vehicle Conference*. IEEE, 2012, pp. 1–8.

[47] R. Bosch, *Bosch Automotive Handbook*, 5th ed. Bentley Publishers, 2002.

[48] A. Levesque and J. Johrendt, "The state of the art of driver model development," SAE Technical Paper, Tech. Rep., 2011.

[49] W. Wang, D. Zhao, W. Han, and J. Xi, "A learning-based approach for lane departure warning systems with a personalized driver model," *IEEE Transactions on Vehicular Technology*, 2018.

[50] Y. Lin, P. Tang, W. Zhang, and Q. Yu, "Artificial neural network modelling of driver handling behaviour in a driver-vehicle-environment system," *International journal of vehicle design*, vol. 37, no. 1, pp. 24–45, 2005.

[51] A. Khodayari, A. Ghaffari, R. Kazemi, F. Alimardani, and R. Braunstingl, "Improved adaptive neuro fuzzy inference system car-following behaviour model based on the driver–vehicle delay," *IET Intelligent Transport Systems*, vol. 8, no. 4, pp. 323–332, 2013.

[52] N. Jalil, N. A. Kheir, and M. Salman, "A rule-based energy management strategy for a series hybrid vehicle," in *Proceedings of the 1997 American Control Conference (Cat. No. 97CH36041)*, vol. 1. IEEE, 1997, pp. 689–693.

[53] M. EPA, "New fuel economy and environment labels for a new generation of vehicles," *Regulatory Announcement EPA-420-F-11-017, US Environmental Protection Agency*, 2011.

[54] U. D. of Energy, *Alternative Fuels Data Center - Fuel Properties Comparison*, 2014 (accessed June 15, 2019). [Online]. Available: https://afdc.energy.gov /fuels/fuel_comparison_chart.pdf